THE 27-28 OCTOBER 1986 FIRE IFO CIRRUS CASE STUDY:

CIRRUS PARAMETER RELATIONSHIPS DERIVED FROM SATELLITE AND LIDAR DATA

Patrick Minnis[1], David F. Young[2], Kenneth Sassen[3],

Joseph M. Alvarez[1], and Christian J. Grund[4]

[1] Atmospheric Sciences Division, NASA Langley Research Center, Hampton, Virginia 23665-5229
[2] Planning Research Corporation, Hampton, Virginia 23666
[3] Department of Meteorology, University of Utah, Salt Lake City, Utah 84112
[4] Department of Meteorology, University of Wisconsin, Madison, Wisconsin 53702

Submitted to
<u>Monthly Weather Review</u>
March 1989

ABSTRACT

Cirrus cloud radiative and physical characteristics are determined using a combination of ground-based, aircraft, and satellite measurements taken as part of the FIRE Cirrus Intensive Field Observations (IFO) during October and November 1986. Lidar backscatter data are used to define cloud base, center, and top heights and the corresponding temperatures. Coincident GOES 4-km visible (0.65 μm) and 8-km infrared window (11.5 μm) radiances are analyzed to determine cloud emittances and reflectances. Infrared optical depth is computed from the emittance results. Visible optical depth is derived from reflectance using a theoretical ice crystal scattering model and an empirical bidirectional reflectance model. No clouds with visible optical depths greater than 5 or infrared optical depths less than 0.1 were used in the analysis.

Average cloud thickness ranged from 0.5 km to 8 km for the 71 scenes. Mean vertical beam emittances derived from cloud-center temperatures were 0.62 for all scenes compared to 0.33 for the Case Study (October 27-28) reflecting the thinner clouds observed for the latter scenes. Relationships between cloud emittance, extinction coefficients, and temperature for the Case Study are very similar to those derived from earlier surface-based studies. The thicker clouds seen during the other IFO days yielded different results. Emittances derived using cloud-top temperature were ratioed to those determined from cloud-center temperature. A nearly linear relationship between these ratios and cloud-center temperature holds promise for determining actual cloud-top temperatures and cloud thicknesses from visible and infrared radiance pairs.

An average visible scattering efficiency of 2.1 was found for this data set. The results reveal a significant dependence of scattering efficiency on cloud temperature. Values of mean scattering efficiency as high as 2.8 suggest the presence of small ice particles at temperatures below 235 K. Large uncertainties in the optical parameters due to cloud reflectance anisotropy and shading were found by analyzing data for various solar zenith angles and for simultaneous AVHRR data. The results highlight the need for additional study of cirrus cloud scattering and remote sensing.

1. Introduction

Accurate quantification of cirrus cloud properties from satellite measurements is particularly important to the understanding of the role of cirrus in climate change. The nonblackness of cirrus at thermal infrared wavelengths renders the interpretation of satellite data taken over cirrus more difficult than measurements over most water clouds. The International Satellite Cloud Climatology Project (ISCCP; see Schiffer and Rossow, 1983) is making an ambitious effort to derive daytime cirrus coverage, altitudes, and optical depths over the globe during a 5-year period. The ISCCP analysis algorithm (Rossow et al., 1988) relies entirely on bispectral data taken at visible (VIS, ~ 0.65 μm) and infrared (IR, ~ 11.5 μm) wavelengths. Although VIS-IR bispectral techniques have been suggested as feasible methods for determining bulk cirrus properties (e.g., Shenk and Curran, 1973; Reynolds and Vonder Haar, 1977), there has been very little application of these techniques to real data prior to the ISCCP.

The basic premise for using the bispectral approach is that the VIS extinction coefficient is related to the IR absorption coefficient. This relationship implies that the cloud VIS reflectance may be used to infer the cloud's IR emittance. Having a value for the clear-sky IR radiance, it is possible to correct the observed cloudy radiance for cloud emittance resulting in an estimate of the radiance emanating from some specified level in the cloud. The equivalent blackbody temperature of this level, usually the cloud center, is then converted to cloud altitude by means of a vertical sounding. The critical relationship ultimately required for this approach is the dependence of IR emittance on VIS reflectance through the IR and VIS optical depths. Since clouds scatter radiation anisotropically, this relationship is also influenced by the viewing and illumination conditions.

The ISCCP cirrus analysis (Rossow et al., 1988) utilizes a combination of theoretical and empirical models to determine the cloud visible optical depth from the observed reflectance, the cloud emittance from the visible optical depth, and finally, the cloud-top temperature from the cloud emittance and the observed infrared radiance. The theoretical cloud model is a radiative transfer scheme which simulates the scattering and absorption of visible radiation by water droplets with an effective radius of 10 μm. For water droplets of this size, the ratio of VIS extinction to infrared absorption is ~ 2.7. An analysis of coincident satellite and lidar data by Platt el al. (1980; hereafter, PRA) and theoretical calculations employing cylinders (Platt, 1979) suggest that this ratio is approximately equal to 2.0 for cirrus. The ISCCP algorithm utilizes the latter value to provide a link between the water droplet model and actual cirrus clouds.

Cirrus clouds are primarily composed of ice crystals with various shapes having maximum dimensions ranging from about 20 μm to 2000 μm (e.g., Heymsfield and Platt, 1984). The scattering properties of hexagonal ice crystals differ considerably from spherical particles (Liou, 1986). Because of the complexities involved in computing scattering by hexagonal solids, cylindrical columns have been used to approximate hexagonal crystals in radiative transfer calculations (e.g., Liou, 1973). More recently, however, Takano and Liou (1989a) have solved the radiative transfer equations for randomly oriented hexagonal plates and columns. Their results are the most realistic to date in that they reproduce certain well-known cirrus optical phenomena.

Absorption plays the dominant role in IR extinction in cirrus clouds. Some theoretical investigations (Liou and Wittman, 1979; Stephens, 1980), however, have shown that scattering effects may also be significant at IR optical depths greater than ~ 0.1. An IR radiance measured by a satellite over cirrus clouds, therefore, is the product of both absorption and scattering processes in the cloud as well as the transmission of radiation from below the cloud (Platt and Stephens, 1980). These effects may complicate the estimation of emittance from the observations. The emittance derived from the satellite data is an effective beam emittance. Some corrections for scattering effects may be needed to obtain the absorption beam emittance which determines the cloud IR optical depth.

Empirical studies have also shed some light on the VIS reflectance - IR emittance relationship. Platt (1973) developed techniques for deriving cloud visible and infrared properties from a ground-based lidar and an upward-looking infrared radiometer. The backscattered intensities measured with the lidar are used to define cloud base and top heights. Cloud emittance was derived from the observed downwelling IR radiance. Platt and Dilley (1979) presented emittance results from a set of observations taken over Australia. PRA used lidar and satellite VIS-IR data to estimate the dependence of cloud beam emittance on cloud VIS reflectance for a limited set of viewing and illumination conditions over Colorado. Their results are more consistent with theoretical scattering from ice cylinders than with scattering from ice spheres. Aircraft radiometric measurements taken over New Mexico (Paltridge and Platt, 1981) have also been used to determine the radiative characteristics of cirrus clouds as related to the cloud ice water path. Those results provide further evidence that real clouds scatter more like cylinders than spheres. Platt (1983) combined the results from previous studies and used them to explain the characteristics of two-dimensional bispectral histograms of VIS-IR data observed from a geostationary satellite. Theoretical calculations of reflectance and emittance for typical cirrus clouds were consistent with the satellite data taken over areas of suspected cirrus clouds. While that study provided encouragement for using a bispectral approach to retrieving cirrus properties from bispectral data, it also highlighted some of the difficulties which are likely to be encountered with such a technique. Platt and Dilley (1984) used lidar and solar radiation measurements to measure part of the single-scattering phase function of real cirrus clouds. Their results fell within the range of laboratory measurements and theoretical calculations for hexagonal crystals. An analysis of a large sample of ground-based lidar and infrared data taken over Australia (Platt et al., 1987) showed that the average emissivity of cirrus clouds is primarily a function of the midcloud temperature. Though fraught with significant uncertainties, that study also indicated that the theoretical value of the ratio of visible extinction to infrared absorption for cirrus clouds may be too low.

From these previous studies, it appears that

(1) cirrus cloud scattering properties are similar to those of hexagonal crystals resulting in reflectance patterns which are unlike those from spheres;

(2) scattering of IR radiation may be important in determinations of IR optical depths; and

(3) the ratio of VIS extinction to IR absorption coefficients is between ~ 1.8 and 4.0.

The full impact of these results on using a VIS-IR bispectral method for retrieving cirrus properties is unknown. Differences between ice crystal and water droplet bidirectional reflectance patterns will introduce errors into the retrieved VIS optical depth. Use of an effective beam emittance with a theoretical model which assumes absorption only may affect the emittance estimation. Finally, uncertainties in the extinction ratio (scattering efficiency) may cause significant errors in the estimation of IR optical depth.

In this paper, the relationship between VIS reflectance and IR emittance is examined using data taken during the First ISCCP Regional Experiment (FIRE) Cirrus Intensive Field Observations (IFO, see Starr, 1987). Ground-based and aircraft lidars are used to define the vertical locations of the cirrus clouds while satellites provide measurements of VIS and IR radiances. Both VIS and IR optical depths are computed from the reflectance and emittance data covering a range of solar zenith angles missed in previous studies. These relationships are derived to provide a means for the application of a bispectral cirrus parameter retrieval algorithm over the FIRE IFO region. Results are presented for the entire IFO period with emphasis on October 27 and 28, 1986. The data presented here also constitute an initial source for developing cirrus bidirectional reflectance models and may be used to help validate the models employed in the ISCCP algorithm.

2. DATA

a. Lidar measurements

Lidar backscatter data were taken from four different sources--three surface and one airborne. The lidars and their operating systems and data products have been described elsewhere. Thus, only a brief description of sources and their uses in this study are given here.

The University of Utah mobile polarization lidar (see Sassen et al., 1989) was located at Wausau, Wisconsin (WAU, 45.0°N, 89.7°W). The NASA Langley ground lidar (Alvarez et al., 1989) was situated at Ft. McCoy, Wisconsin (FMC, 43.9°N, 90.8°W), while the University of Wisconsin high spectral resolution lidar (Grund and Eloranta, 1989) was in Madison (MAD, 43.1°N, 89.4°W). These ground systems acquired nearly continuous lidar backscatter profiles during the cirrus days of the IFO with especially good coverage during the case study period. The lidar returns are used to define the cloud base and physical thickness. Under conditions of small attenuation and constant backscatter phase function, the backscatter intensity profiles indicate the vertical distribution of cloud extinction. A time series of these lidar returns shown in Fig. 1 define the outlines of the cirrus clouds as they passed over FMC during the afternoon of October 28. Solid black areas define the most intense cloud backscatter. Grey denotes less backscatter and white indicates no cloud. Vertical stripes represent missing data. Cloud-top altitude is fairly constant at ~ 11 km. Cloud base changes from ~ 8 km to 10 km approximately every half hour. In the morning, cloud base was observed at ~ 7 km, while cloud top varied between 8 km and 11 km. A similar variation is also seen in the WAU estimated volume backscatter coefficients, β_π, shown in Fig. 2 for the morning of October 28.

Darker portions of the plot correspond to higher values of β_π. The particle backscattering efficiency depends on cloud particle shape and phase. Further details of the lidar returns are reported in the cited references.

Three parameters are derived from plots like those in Figs. 1 and 2 by averaging the data within ± 15 min of the GMT (Greenwich Mean Time) half hour plus 5 minutes. All times, however, will be given here to the nearest half hour. Cloud-top altitude, z_t, and cloud-base altitude, z_b, are defined as the average altitudes of the highest and lowest nonclear-air backscatter returns, respectively. Similarly, the cloud thickness is $h = z_t - z_b$. Mean cloud height (approximately cloud center height), z_c, is the backscatter-intensity weighted average height of the cloud. It corresponds roughly to the altitude below which 50% of the lidar backscatter is accumulated. These parameters were estimated graphically for the FMC and WAU sites, while a computer analysis was applied to the MAD results. The value of z_c for MAD corresponds to the midpoint in optical thickness independent of cloud attenuation (see Grund and Eloranta, 1989). Since the clouds are advecting over the fixed surface sites, the averaged lidar data correspond to a thin vertical cross-section taken out of some cloud volume. It is assumed that the cross-section-averaged data represent the mean conditions of that volume.

These same parameters were also derived from the down-looking lidar backscatter plots reported by Spinhirne et al. (1988) for selected flight tracks of the high-flying, NASA ER-2 aircraft over the IFO area. Shorter time averages were used since the plane's motion greatly increased the cirrus advection rates relative to the lidar. In some instances, the clouds were too thick for complete penetration by the ground-based lidars. To determine these occurrences, the cloud altitudes estimated from the ground were compared to those determined from the nearest aircraft flight. On most days, there was good agreement between the surface and airborne lidars. The thick clouds observed on October 22 required use of the aircraft lidar to obtain a good estimate of z_t. At other times when no aircraft data were available for comparison, a different approach was used to estimate z_t (see Sec. 3a).

b. Temperature data

Soundings from Green Bay, Wisconsin, were used to determine temperature-height relationships for all of the data. Linear interpolation was used to estimate half-hourly soundings from the 6-hourly data . Cloud-top temperature, T_t, corresponds to z_t on the soundings. Mean cloud temperature, T_c, is found from z_c. Surface temperatures taken every 6 hours at MAD, WAU, and Lone Rock, Wisconsin (Hahn et al., 1988), and occasionally at the FMC site were used to supplement the clear-sky temperatures derived from the satellite data (see Sec. 3b).

c. Satellite radiances

Half-hourly VIS and IR data from the Geostationary Operational Satellite (GOES) were resolved to 4-km pixels by averaging and replication of 1-km VIS and 4-km x 8-km IR pixels, respectively, for most times. When the full-resolution data were not available, 8-km pixels derived by pixel averaging (VIS) and sampling (IR) were used. The pixels were navigated to ± 8 km as in Minnis and Harrison (1984a). Pixel pairs were extracted for areas within 0.35° longitude and 0.25° latitude of the surface lidar sites. These areas correspond to cloud advection at wind speeds of ~ 30 ms^{-1} for a half-hour interval. Strips of pixels, 4 (2) pixels wide, corresponding to the wind vector at z_c centered over the surface site were then taken from the 4-km (8-km) resolution areas. The satellite data corresponding to the ER-2 flight track were extracted for a strip centered on the flight track. This strip is approximately 30 km wide and 100 km long.

Two-dimensional histograms of the VIS and IR radiance pixel pairs were formed from the strips of extracted data. The VIS data, stored as counts, D (where $0 < D \leq 63$), in the histogram, were converted to radiance and VIS reflectance, ρ, using the calibration of Whitlock et al. (1989). The raw IR data are given as equivalent blackbody temperatures, T, and are converted to radiance with the Planck function, B(T), evaluated at 11.5 μm. Note that all radiometric quantities discussed in this study are spectral quantities, either VIS or IR, so no subscripts denoting spectral dependence are given.

A similar set of histograms was derived from the NOAA-9 Advanced Very High Resolution Radiometer (AVHRR) Global Area Coverage (GAC) 4-km data. The NOAA-9 daytime pass over the areas occurred between 2000 and 2130 GMT (~ 1430 local time). Radiances from channels 4 and 5 were averaged to produce an IR radiance close to that of the GOES. The AVHRR VIS data were taken from channel 1 and converted to reflectance using the calibrations of Whitlock et al. (1989, personal communication).

Solar zenith, satellite zenith, and relative azimuth angles, θ_0, θ, and ψ, respectively, were computed for each set of measurements. The only GOES available at that time was GOES-6 located over the Equator at approximately

97°W. This location yields a value of $\theta \sim 52°$ for the ground sites. Relative azimuth angles were confined to the backscattering hemisphere for GOES. The orbital precession of the NOAA-9 produces a variation in θ between 0° and 70° over a given site every 4-5 days. Because of its cross-track scan pattern, the AVHRR views a given site from relative azimuth angles which lie in both the forward and backward hemisphere at a nearly constant skew to the solar plane. The skew depends on both the solar and site latitudes. Consequently, a range of solar zenith angles with relatively constant viewing angles is covered using the GOES, while a range of viewing angles at a constant θ_0 is covered with the AVHRR.

Days when cirrus were observed over the IFO without substantial low-cloud interference are referred to as cirrus days. The times used in this study when lidar and satellite data coincided with cirrus are listed in Table 1.

3. Methodology

a. Emittance

The effective cloud beam emittance is given here as

$$\epsilon_b(\theta) = [B(T) - B(T_s)]/[B(T_z) - B(T_s)], \qquad (1)$$

where T_z is the temperature at some altitude z corresponding to the cloud. The mean clear-sky equivalent blackbody temperature over the area of interest, T_s, has a weak dependence on θ. The effective beam emittance includes the effects of scattering as noted earlier.

Cloud beam emittance is calculated twice for each set of lidar-radiance data using $T_z = T_c$ and $T_z = T_t$. The former value, which corresponds to the quantity used in most previous studies (e.g., PRA), may be more representative of the actual radiating part of the cloud. It is unlikely that a value of $\epsilon_b = 1$ will be measured at a useful satellite zenith angle using T_t because of the low density of particles in the upper portions of the cloud. On the other hand, T_c may be too great for some thick cirrus clouds. In those cases, $\epsilon_b > 1$. Although effective beam emittances greater than unity may be possible due to scattering enhancements of the upward radiance (Platt and Stephens, 1980), the uncertainties in z_c for thick clouds preclude any definitive measurements of $\epsilon_b > 1$. Thus, if $\epsilon_b > 1$, T_c is decreased until the average value of ϵ_b for a given reflectance is less than or equal to one.

During initial processing of the data, it was determined that the maximum emittance found using T_t was ~ 0.86, except for those cases with cloud cover too dense for complete penetration of the lidar beam. To identify and correct the exceptions, a new estimate of T_t was computed whenever T_c was adjusted as explained above. This new estimate,

$$T_t' = B^{-1}\{B(T) + [B(T) - B(T_s)] / 0.86]\},$$

was then compared to T_t. If $T_t' < T_t - 3K$, then $T_t = T_t'$. The result was then compared to the tropopause temperature. If T_t was colder, it was set equal to the tropopause temperature. The value of z_t was then adjusted to correspond to the value of T_t.

It is also assumed that

$$\epsilon_b = 1 - \exp(-\tau_e/\mu), \tag{2}$$

where τ_e is the effective IR optical depth and $\mu = \cos\theta$. Based on the results of Platt and Stephens (1980), it is expected that the viewing zenith angle dependence of ϵ_b will not depart significantly from (2). Values of effective beam emittance derived with AVHRR data may be adjusted to the GOES viewing zenith angle with this relationship.

The vertical effective beam emittance from (2) is

$$\epsilon_a = 1 - \exp(-\tau_e). \tag{3}$$

It is assumed here that scattering effects are negligible in the upwelling direction. Thus, τ_e is equivalent to the IR absorption optical depth and ϵ_a is equal to the vertical emittance. This assumption is consistent with the inability to confidently obtain $\epsilon_b > 1$ with the current data set.

b. Clear-sky temperature and reflectance

The clear-sky temperature is estimated in several different ways. The first order estimate is taken from the initial results of Minnis et al. (1989) which applies the techniques of Minnis et al. (1987) to 0.5° regions within the greater IFO area (42°N - 47°N, 87°W - 92°W). That approach sets a VIS threshold ~ 2 counts above the clear-sky reflectance, ρ_s, or count, D_s. All pixels which are darker than this threshold and have $T > T_{max} - 3$ K are considered to be clear. Their average is T_{cs}. The surface air temperatures, T_g, are also taken from nearby ground stations. A rough correction is applied to these temperatures to adjust for atmospheric attenuation and the difference between the temperature of the surface skin and the air at shelter height. The resulting estimate of clear-sky temperature is T_a. An example of the relationship between T_{cs} and T_g is shown in Fig. 3 for a region including FMC during October 27, 1986. Note that the difference between T_{cs} and T_g constitutes the correction to determine T_a from T_g. It varies with local time from positive values in the morning to negative values in the afternoon. This variation is typical of land surfaces (e.g., Minnis and Harrison, 1984a).

The initial value of T_{cs} for the ground site is compared to the values for the surrounding regions to check for cirrus contamination of the clear-sky temperature. If T_{cs} for the ground site is not within 2 K of the warmest value found for nearby regions, then its value is reset to that of the warmest value. Normally, $T_s = T_{cs}$. If extensive overcast prevents the calculation of T_{cs}, $T_s = T_a$.

The AVHRR clear-sky temperatures are first estimated using T_{cs} derived from the AVHRR data. If that result is lower than the corresponding GOES estimate of T_s by 2K, then the AVHRR value of T_{cs} is reset to the GOES value. Since the value of T_s should vary by only 1 or 2 K over the range of θ used here, limb-darkening effects are assumed to be negligible in the AVHRR analysis.

Values of clear-sky reflectance, ρ_s, were computed for each region using the 0.01° clear-sky albedo, α_s, map of the IFO area constructed by Minnis et al. (1989) from GOES data at each half hour. Clear-sky reflectance over any latitude, λ, and longitude, ϕ, of the grid at time, t,is estimated as

$$\rho_s(\lambda,\phi,t,\theta_0,\theta,\psi) = \alpha_s(\lambda,\phi,t,\theta_0)\chi_s(\theta_0,\theta,\psi), \tag{4}$$

where χ_s is the anisotropic reflectance factor with values given by the model of Minnis and Harrison (1984b). The value of θ_0 varies by a few degrees over the IFO time period, while the values of α_s were normalized to a single value of solar zenith angle designated θ_{0t}. To account for these variations, $\alpha_s(t,\theta_0) = \alpha_s(t,\theta_0)\mu_0/\mu_{0t}$, where $\mu_0 = \cos\theta_0$ and $\mu_{0t} = \cos\theta_{0t}$. The clear-sky diffuse albedo is

$$\alpha_{sd} = \int \alpha_s(\theta_0)\mu_0 d\mu_0 \Big/ \int \mu_0 d\mu_0 ,$$

integrated over $\mu_0 = 0,1$. The value of α_{sd} is estimated to be equal to the value of $\alpha_s(57°)$ in this study.

c. Cloud reflectance

Cloud reflectance, ρ_c, is estimated with a variant of the simple physical model used by PRA. That is,

$$\rho = T_a\rho_c + \rho_s T_c T_u + \alpha_{sd}(1 - \alpha_d)(1 - T_c - \alpha_c), \qquad (5)$$

where ρ is the measured reflectance, α_c is the cloud albedo at θ_0, χ_c is the anisotropic reflectance factor for the cloud, and $\rho_c = \alpha_c\chi_c(\theta_0,\theta,\psi)$. The transmittance of the air above the cloud is

$$T_a = \exp[-k_o u(1/\mu_0 + 1/\mu)],$$

where $k_o = 0.085 - 0.00052u$ (Rossow et al., 1988) and u is the ozone abundance in cm-STP. The value used here, $u = 0.32$ cm-STP, is the average of the midlatitude winter and summer standard atmospheres above 10 km from

McClatchey et al. (1973). PRA implicitly assumed that $T_a = 1$, although there is significant ozone absorption in the Chappius bands.

The transmittance of the cloud to direct solar radiation at θ_0 is

$$T_c = \exp(-\tau_v / 2\mu_0), \tag{6}$$

(see PRA). Similarly, the direct transmittance from the surface through the cloud along the satellite line of sight is

$$T_u = \exp(-\tau_v / 2\mu).$$

The visible optical depth is reduced by a factor of two for the direct transmittance because at least half of the radiation scattered out of the beam is actually diffracted in the forward direction (Takano and Liou, 1989a). Clear-sky reflectance along the satellite line of sight is ρ_s, and α_{sd} is the effective clear-sky albedo to diffuse radiation directly below the cloud. Due to the relative homogeneity of clear-sky reflectance over the IFO region, it is assumed that α_{sd} and ρ_s may be computed from the same data. The albedo of the cloud to diffuse radiation is α_d.

This model assumes that all of the ozone absorption occurs above the cloud (first term) and that all Rayliegh and aerosol scattering is confined to the layers below the cloud. The second term in (5) accounts for direct solar radiation which passes through the cloud, reflects from the surface, and passes back through the cloud in the direction of the satellite. The third term accounts for the radiation which passes down through the cloud via multiple scattering, reflects from the surface (which now acts as a Lambertian surface) below the cloud, and returns through the cloud scattered in the direction of the satellite.

In addition to values for the clear-sky terms, solution of (5) for ρ_c requires specification of τ_v and χ_c. Here, the value of the VIS optical depth is estimated by iteration on (5) using a log-linear interpolation of the relationships between μ_0 and α_c for randomly oriented hexagonal columns (length, 125 μm; width, 50 μm) in Fig. 4 of Takano and Liou (1989b). Similar interpolations are used to estimate $\alpha_d(\tau_v)$, where

$$\alpha_d(\tau_v) = \int_0^1 \alpha_d(\tau_v,\mu_0)d\mu_0 \;/\; \int_0^1 \mu_0 d\mu_0 .$$

Given a measurement, (5) may be solved for an initial guess of cloud albedo by assuming that $T_c = T_u = 1 - \alpha_c$. A value for τ_v is determined from this initial guess using the theoretical data. It is then used in (5) to solve for α_c. The initial guess and resulting value of α_c are compared. If the absolute difference is greater than 0.001, the iteration proceeds using the new value of α_c as the guess. A limit of 20 iterations is imposed, although fewer than 5 iterations are required to achieve a difference of $\pm$ 0.001 between the guess and the computed value of α_c for most cases. Since α_c may be greater than zero, even for $\rho \leq \rho_s$, α_c is set to 0.001 for initial guesses which are less than or equal to zero. If $\tau_v < 0$, $\alpha_d < 0.001$, or $\alpha_c \leq 0.001$ after any iteration, it is assumed that τ_v is indeterminate and the data are not used.

A value for χ_c is needed to determine α_c from ρ_c. χ_c depends on τ_v and the cloud microphysics. No models of χ_c are currently available for ice clouds in terms of τ_v. Because of favorable angles PRA were able to assume that $\chi_c = 1$. Most empirical and theoretical bidirectional reflectance models for cloudy scenes (e.g., Suttles et al., 1988), however, reveal a systematic decrease in χ_c with θ_o for the angles used in this study. The cloudy scene bidirectional reflectance model developed by Minnis and Harrison (1984b) is used to estimate χ_c. That model was derived for top-of-the-atmosphere (TOA) broadband shortwave reflectance from clouds of all types. It is assumed that the broadband reflectance patterns are the same as those in the VIS regime. This model's reflectance anisotropy is similar to other empirical and theoretical models (Stuhlmann et al., 1985). The inclusion of all cloud types in its derivation should produce a reflectance pattern between those for ice and liquid water clouds.

Examples of the variations of ρ as a function of α_c computed with (5) are shown in Fig. 4a for WAU at 1400 and 1800 GMT. The corresponding values of ρ_s are 0.13 and 0.16, respectively, with $\alpha_{sd} = 0.11$. The relationship between cloud albedo and optical depth depends on the solar zenith angle resulting in a divergence of the curves at larger values of α_c. Additional calculations were performed for $\mu_0 = 0.4$, $\chi_c = 1$, and $\rho_s = 0.04$, 0.08, 0.16, 0.32, and 0.64 with $\alpha_{sd} = 0.92\rho_s$. The results are shown in Fig. 4b. For relatively dark surfaces, the measured reflectance increases monotonically with α_c. Over bright surfaces, the reflectance actually decreases first, then increases at greater cloud albedos. A dark surface contributes little to the upward flux, while the opposite is true for bright surfaces. The increased reflectance of a cloud to diffuse radiation tends to trap some of the reflected radiation from the surface. For thin clouds over bright surfaces, this effect can result in a reflectance which is lower than that observed for the clear-sky case. Additional calculations for other solar zenith angles indicate that the insertion of the thin cirrus cloud above the bright surface decreases the albedo at lower sun angles making the discrimination of clear and cloudy skies more difficult over deserts and other bright scenes. It is possible that this effect may also be important at certain angles and values of χ_c over dark surfaces.

d. Scattering-to-absorption ratio

The mean VIS scattering to IR absorption optical depth ratio

$$r = \sum_{i=1}^{N} (\tau_v / \tau_e)_i / N \qquad (7)$$

is computed for each value of ρ. This parameter is equivalent to the scattering efficiency factor. Only one temperature is used to compute τ_e for a given data set since only one average cloud height is derived for each time. Changes in the actual cloud height and thickness within the scene (e.g., Fig. 1) tend to introduce variations in τ_e for a given reflectance. A mean value of r is computed for each cloud reflectance value to minimize the effects of cloud height variability.

If it is assumed that $\alpha_c \propto \tau_v$ for small optical depths, then

$$\epsilon_b = 1 - \exp(-k\alpha_c/\mu), \qquad (8)$$

where k is the constant of proportionality. This relationship is primarily used here to filter low clouds. Values for k are determined in the following manner. For a given site and time, ϵ_b is computed with (1) for each pixel with $D > D_s$ and $T < T_s - 3$ K. The mean emittance is then computed for each value of D corresponding to a value of α_c. Equation (8) is solved for k using each albedo-emittance pair. An average value of k is then computed for a specified subset of the data. This procedure is applied using both $T_z - T_t$ and $T_z - T_c$.

e. Low and thick cloud filtering

The presence of low clouds contaminates the data since the analysis is predicated on the presence of only one cloud layer (it may contain two or more distinct sublayers). The cloud heights are defined for the upper-level cloud (generally, $z_b > 4$ km) detected by the lidar. In some instances, the occurrence of low clouds was either noted by the lidar operators or evident in the backscatter intensity plots. In other cases, the visual observations were not recorded or the low clouds were located within the satellite-defined area around the site, but beyond the observer's horizon. The data sets containing low clouds must either be eliminated or the pixels contaminated by low clouds must be removed. Elimination of all data sets containing low clouds would substantially reduce the number of samples.

To filter the data, it is assumed that low clouds are generally brighter than cirrus, but their emittances depend on albedo, as in (8), in the same manner as cirrus. Thus, if a maximum cloud albedo is known for a given cirrus emittance, then it may be assumed that any pixels brighter than that maximum contain some low clouds. The values of those maximum albeods, α_{max}, must be estimated here. To determine those maximum values, the histograms were first filtered manually to obtain a set containing no low clouds. The maximum albedo for each temperature (emittance) was extracted for every histogram at a given GMT. Data taken on October 22, 1986, were used in the analysis. All maxima for a given GMT were compared to determine the greatest values for that time. Very little dependence on GMT was found in this comparison. Therefore, the maxima from all hours were combined. The resultant values were then used to solve (8) for k. The results were averaged to obtain the coefficient, k_{max}, which is used to define the maximum cloud albedo for a given emittance. The results of this process yield $k_{max} = 2.4$ for $T_z = T_c$ and $k_{max} = 2.0$ for $T_z = T_t$. Thus, for a given time, (8) may be solved for α_{max} using k_{max} and the emittance. Any pixel with $\alpha_c > \alpha_{max} + 0.025$ is assumed to contain low clouds and is eliminated from further processing.

An example of this filtering is shown in Fig. 5 for the data over FMC at 1930 GMT, October 28, when low clouds were noted in the observer's log. Crosses represent individual pixels. The solid line represents α_{max} computed using k_{max}. The vertical dashed line, $\alpha_{max} = 0.20$, is used at low reflectances because of large uncertainties at those reflectance levels. The filtering process eliminates the pixels which clearly contain low clouds (i.e., those to the right of the line). Some pixels containing both low and high clouds, however, may remain in the data.

All cases having $\tau_v > 5.0$ were also removed from the data set. This arbitrary limit was imposed to minimize the uncertainties in τ_e, τ_v, and subsequent values of r. The error in derived optical depth increases with increasing emittance. The value of T_c is also more uncertain for thick clouds than thinner clouds. Thus, errors in emittance are greater for these thick clouds. Their removal does not significantly affect the trends in the results. Inclusion of the thick clouds, however, greatly increases the noise in the data. No case study scenes were affected by this filtering.

f. Partially cloud-filled pixels

The use of (7) or (8) implicitly assumes that the pixel is completely filled with cloud. While it is likely that some of the pixels are partially clear, definitive means for determining which are overcast and which are partly cloudy are unavailable. Platt (1983) proposed a bispectral method to discriminate partly cloudy pixels from those containing thin clouds. His technique requires uniform blocks of constant height and thickness for detection of partly cloudy pixels. Detection of thin clouds allows variable thicknesses, but not heights. As seen in Figs. 1 and 2, real cirrus clouds are anything but uniform and constant in altitude and depth. An actual cloud field may also contain broken clouds with variable optical depths. The nonuniformity of such real clouds blurs the distinction between the linear relationship for partly cloudy pixels and the exponential dependency for variable thickness overcast pixels. For consistency with the ISCCP algorithm, it is assumed here that the pixels colder than T_{max} - 3 K are overcast. The data are not used, however, if there is evidence of any significant breaks in the ceiling from the lidar displays. Very few breaks were seen over the sites on October 28. The cirrus observed on October 27 were mostly scattered leading to the selection of only two scenes for that day.

4. Results

a. GOES emittances for midcloud temperature

All results discussed in this section are based on $T_z = T_c$ in (1). Examples of the two-dimensional histograms used in this analysis are shown in Figs. 6a and 6b for 1500 GMT over FMC. The latter represents a cirrus case (see Fig. 1) on October 28, while the former, taken during the previous day, is typical of clear conditions. Maximum clear-sky reflectance for this hour is denoted with the dashed line in Fig. 6a. Some of the cold, apparently cloudy pixels in Fig. 6b are no brighter than the clear pixels in Fig. 6a. Moreover, some of these pixels are actually darker than the cloud-free pixels. Depending on χ_c and τ_v, some of the cold, dim pixels yield a positive value of α_c in the solution of (5). Those pixels with $\alpha_c \leq 0$ or $T < T_s$ - 3K are, hereafter, referred to as "dark" pixels. They are not used to solve either (7) or (8). Their impact and origins are discussed in a later section. The cloud emittances are plotted in Fig. 7a against the measured reflectances for the case in Fig. 6b. Eliminating the "dark" pixels and applying (5) to the data in Fig. 7a yields the pixels values shown in Fig. 7b for cloud albedo. Averaging the emittances for a given albedo produces the mean values plotted in Fig. 7c. The solid line represents (8) using the average value of $k = 5.1$. The mean effective emittance and visible optical depths for the data used in Fig. 7c are $\bar{\epsilon}_b = 0.38$ and $\bar{\tau}_v = 0.59$, respectively, yielding $r = 1.73$.

The data from FMC in Fig. 7c for this hour are compared to those from MAD and WAU shown in Fig. 8. Apparently, the clouds over WAU are much denser than those over MAD while the MAD observations are similar to those over

FMC. Values of T_c differed by only 1 K among the sites, while T_t ranged from 225 K at WAU to 217 K at MAD. Depolarization ratios derived from the lidar returns indicated intermittent liquid layers during the morning of October 28, especially at ~ 1500 GMT. The data from all three sites were combined, averaged, and fit with (8) yielding $k = 5.6$. Averaging the optical depth ratios for all three sites yields $r = 2.01$. The scatter in the means between the sites at a given hour is of the same order as that for different hours at the same site as seen in Fig. 9 for FMC at 3 times during October 28.

A summary of the results for the Case Study (October 27-28), hereafter referred to as CS, are given in Table 2. Cloud optical depths were much greater over WAU than over the other sites. The percentage of dark pixels was higher over FMC and MAD than over WAU. Cloud-top heights range from 9.5 to 11.0 km at all three sites. The cloud-center temperatures vary by about 25 K.

Due to dropouts, the only data available for 1500 GMT during the primary IFO cirrus days occurred on October 28. Data from other days were available for most of the afternoon hours. For example, the cloud albedo-emittance pairs taken at 2000 GMT (Fig. 10) cover the full range of emittances. All of the data used in the analysis for the CS are shown in Fig. 11a. The clouds over the area during October 27 and 28 were generally much thinner with lower emittances than most of those observed during the other days. Combining data for all of the times given in Table 1 produces a large number of samples for $\epsilon_b < 0.5$ and $\epsilon_b > 0.8$. No data are found for $\epsilon_b < 0.08$ since no clouds are recognized if $T > T_s - 3$ K.

Table 3 summarizes the values of τ_v and r derived from all of the IFO data (Fig. 11b) and from CS data only (Fig. 11a) for each relevant GMT. The average scattering angle, Θ, between the sun, satellite, and scene is also listed in Table 3. Visible optical depths observed during the CS are less than half of those observed for all of the IFO cirrus days. Despite these and other differences, two similarities are quite evident. For both data sets, the scattering efficiency appears to increase with decreasing θ_0 and increasing Θ. At high values of θ_0, r is well below the expected limit of 2. The average values of r are also very close, 2.07 and 2.08, for the CS and IFO, respectively.

The various values of VIS and IR optical depths derived from Fig. 11 were averaged for discrete levels of τ_e. Figure 12 shows the variation of mean r with IR optical depth. The standard deviations are denoted with the vertical lines. The CS data (squares) vary from 1.62 to 2.55, while the IFO data vary range from 1.60 to 2.31. There is good consistency between the IFO (circles) and CS results for $\tau_e < 1.0$. Clouds with $\tau_e > 1.0$ were undersampled during the CS (Fig. 11a). The trend of decreasing values of r with τ_e for $\tau_e < 1.0$ may be due to dark pixel effects (see section 5c).

Average scattering efficiencies were also computed for discrete levels of T_c. They are plotted in Fig. 13. The value of r is close to 2.0 for $T_c > 235$K. Maximum values of r, approximately 2.8 for both data sets, were found for $T_c \approx 225$ K. The lower value of r for $T_c = 217$ K is derived from only five cases which were mostly taken during the late afternoon.

The mean vertical beam emittance is given as a function of temperature in Fig. 14. Although there is a general increase in ϵ_a with increasing cloud temperature, the values derived for the CS are generally lower than the IFO means. Cloud thickness versus T_c is shown in Fig. 15. Maximum average thickness is found at $T_c \approx 232$ K for the IFO and at $T_c \approx 241$ K for the CS. The CS values of h increase nearly monotonically with T_c. The IFO results show a tendency towards thinner clouds for $T_c < 220$ K and for $T_c >$ 240 K. The thickest clouds were observed during October 22 and November 1. Cloud IR volume absorption coefficient, $\sigma_a - \tau_e / h$, is plotted against T_c in Fig. 16. The results reveal a trend of increasing extinction with T_c in the IFO data (correlation coefficient of 0.71). The average value of σ_e is 0.20 for the CS data.

b. GOES emittances for cloud-top temperature

The analyses discussed above were also performed for the GOES-derived emittances for $T_z - T_t$. A plot of all of the mean cloud emittance-albedo pairs is shown in Fig. 17. The largest concentrations of data are found for $\epsilon_b(T_t) < 0.8$. In general, α_c is greater for a given value of ϵ_b than it is in Fig. 11b. Cloud-top emittance tends to plateau at $\epsilon_b \approx 0.89$, while cloud-center emittance appears to level at $\epsilon_b \approx 0.98$. The lower emittances lead to diminished values of τ_e and greater values of r relative to those derived for T_c.

The emittance ratio, $r_\epsilon = \epsilon_b(T_t) / \epsilon_b(T_c)$, was computed for discrete intervals of T_c. Mean values and standard deviations of these ratios are shown in Fig. 18. The emittance ratio increases almost linearly with decreasing cloud center temperature. Standard deviations about a given mean ratio are less than 0.1. The emittance ratio is close to unity for $T_c <$ 215 K.

c. GOES/ER-2 cloud parameters

Table 4 lists the data and derived parameter values for the five cirrus matches between the GOES and ER-2 lidar for the CS days. Data taken during October 27 was located just outside the northwestern boundary of the IFO area. On October 28, the ER-2 was over Lake Michigan at ~ 1600 GMT, while it was near FMC at 1800 GMT. The three scenes at 1600 GMT correspond to small contiguous areas. The scattering efficiencies follow the same trends observed for the ground sites with the greatest values of r near local noon. The average value of r over the lake at 1600 GMT is 2.1, a value very close to that observed over land for 1600 GMT (see Table 3).

d. Cloud parameters from AVHRR data

Figure 19 presents the averaged cloud emittance-albedo pairs derived from both AVHRR and GOES data taken over WAU on October 28. Although the relative viewing angles were within ± 8° for the two satellites, the absolute viewing conditions were different. The GOES viewed the region from the south while the AVHRR viewed from the north. The solar plane was almost midway between the two orbiters. Discrepancies in the albedo range may be due to this misalignment (more dark pixels were found in the GOES results).

Resolution differences, however, would tend to produce a smaller range in both albedo and emittance for the GOES (8-km) relative to the AVHRR (1 x 4 km^2) radiances as observed in Fig. 19. In general, the GOES data are very close to the AVHRR results except for the smaller values of α_c. The latter may be affected by the presence of "dark" pixels.

Another comparison of GOES and AVHRR results is given in Fig. 20 for data taken over WAU November 2. The AVHRR viewed the scene with $\theta = 18°$ and $\psi = 38°$. The squares correspond to AVHRR data as reduced for the given viewing angles. AVHRR emittances corrected to the GOES viewing zenith angle with (2) are denoted with the crosses. The range in α_c is smaller for GOES than for the AVHRR consistent with the resolution differences. In this case, the AVHRR data produce a much lower minimum cloud albedo. The application of (2) appears to have produced very similar emittances for the two data sets.

All of the coincident AVHRR and GOES data are summarized in Table 5. The AVHRR infrared optical depths are all slightly greater than the corresponding GOES values, while the differences in τ_v vary from scene to scene. Even when the times and angles are very close and the data appear similar as in Fig. 19, there are substantial differences in τ_v and r. Over FMC during the 28th, there is good agreement between the parameters, however. The outstanding differences may be attributable to a number of factors discussed below.

e. Uncertainties

The parameter values derived here are subject to considerable uncertainty as evidenced by the results in Table 5 and the large standard deviations in earlier figures. Potential sources of error abound in an analysis of this type due to the large number of variables and the nonuniformity of cirrus clouds.

Parameters derived from the lidar essentially provide a two-dimensional view of the cirrus clouds. The assumption that z_c, h, and z_t represent the average cloud heights within the large areas covered by the strip of pixels is difficult to evaluate. One means of estimating how well the lidar data represent the large area cloud characteristics is to examine the differences between the strip of pixels and surrounding areas. The rms difference between the emittances for the strip and the box containing the strip is 0.05 or 7%. This difference is equivalent to a ± 0.7 km variation in cloud center height between the strip and the box. Changes of 2 km in cloud center altitude during a given half hour are common as seen in Fig. 1. It appears that the variations in the small scale lidar data are greater than those in the large scale satellite data.

Assuming that the large scale differences are representative of the lidar-satellite scale differences, it is estimated that the use of lidar data to set z_c causes an uncertainty in ϵ_a of ± 10% based on an average value for ϵ_a of 0.62. The accuracy will probably be less for lower, thicker clouds and slightly greater for high, thin clouds. The latter are better defined in the lidar data and present more contrast to the satellite view than the former. Note that no clouds with $\epsilon < 0.1$ were included in the analysis. A conservative estimate of the uncertainty in T_s is ± 2K.

Inclusion of this error raises the overall uncertainty in ϵ_a to ± 13%. This uncertainty in ϵ_a is equivalent to a ± 20% uncertainty in τ_e for a given scene. The average IR optical thickness is 0.96 for all 71 scenes. From the strip and box comparison, it is also estimated that z_t and h have uncertainties of ± 0.7 km.

Another source of uncertainty in ϵ_a is the use of a mean cloud height for the entire scene. This error source may be examined by performing a pixel-by-pixel analysis on a scene which varies systematically with time. One example is the cloud over FMC between 2020 and 2050 GMT. The GOES pixels from the corresponding wind strip data were averaged in lines perpendicular to the wind vector. Using the wind speed, these averaged pixels were converted to times and aligned with the lidar-defined cloud parameters. The results shown in Fig. 21 indicate good alignment between the two data sets. It appears that, in this case, the lidar data provide an accurate cross section of the cloud. The GOES reflectance increases as the cloud thickens and T increases as z_c lowers. Equations (1) and (5) were applied to each average pixel using T_c derived from Fig. 21 to determine τ_e and τ_v. Figure 22 shows the variation of the parameters with time. Although the thin part of the cloud is detected with the IR data, a value for τ_v is not computed since the reflectances are lower than that for clear skies. Nevertheless, the mean values for τ_e and ϵ_b derived on a pixel-by-pixel basis are 0.59 and 0.54, respectively, compared to 0.62 and 0.59 derived for the entire scene using a mean value of z_c. This comparison suggests that the error in ϵ_b for using the mean cloud height is around 10%. While these results may not represent all cases, they indicate that the use of a mean cloud height for the analysis is a reasonable approach.

Assessment of the accuracy of τ_V relies on the satellite data and the models used to solve (5). The two greatest sources for error in (5) are the bidirectional reflectance model and the theoretical cloud albedo model. The latter is based on a set of calculations for one typical set of microphysical properties. While the scattering phase function should not vary significantly for hexagonal ice crystals of various sizes, other shapes and phases such as bullet rosettes or water droplets may occur in the observed clouds. Thus, some uncertainty arises from the use of the specific model. Another source of uncertainty is the interpolation scheme used to extract τ_V from a set of four curves defining the relationship of τ_V and α_c as a function of θ_0. It is estimated that the use of the log-linear interpolation for a given θ_0 is accurate to about ± 5% for the solar zenith angles used here.

The anisotropy of the reflected radiation field for real clouds depends on the optical thickness, incident radiation, microphysical properties of the cloud, and the morphology of the cloud field. The value of χ_c used here is fixed for a given set of angles and represents an empirical average for all cloud types. Since cirrus clouds are the only type considered here and the angles are fixed for a given hour, it is likely that χ_c will be biased with respect to local time. There will also be random errors in χ_c due to variations in microphysics, morphology, and cloud optical depth for a given hour. The magnitudes of these errors are currently unknown, but are potentially large. If it is assumed that the time sampling represents a random sampling of χ_c, however, then averages of various parameters derived from all times should minimize the effects of biases in χ_c.

The bidirectional reflectance model errors are estimated by reanalyzing the data using $\chi_c = 1$. The resulting overall mean value of r is 1.9, less than the value of 2.0 expected for large particles. The rms change in χ_c of ± 10% results in an 8% decrease in r and an rms difference of 18%. Values of r near midday are increased relative to the nominal results, while those in the early morning and late afternoon are decreased. Since the range in r is reduced by using the models, it may be concluded that their application was appropriate for this data set.

The dispersion of the nominal ratios, however, is significant on an hourly basis even when the models are used. If it is assumed that r is independent of time, then mean values of χ_c may be determined from (5) if r and τ_e are known. The data were reanalyzed forcing the scattering ratio to a value of 2.08 and solving (5) for χ_c. Resulting mean hourly values for χ_c are given in Table 6 with the nominal values from the bidirectional reflectance model. The results indicate more anisotropy in the cirrus reflectance pattern than in the empirical model for all cloud types. From these results, it may be concluded that the bidirectional models are accurate to within ± 20%.

5. Discussion

a. Infrared parameters

The CS results in Fig. 14 are very similar to those derived by Platt et al. (1987; hereafter, PSD) from ground-based observations in Australia. The mean value of ϵ_a is 0.33 for the CS, the same as that found by PSD for their midlatitude site. The variation of vertical beam emittance with T_c for the IFO data probably differs from that for the CS and the PSD data because of substantial differences in cloud depths. Clouds observed during the CS were 2.6 km thick on average compared to a mean thickness of 4.2 km during the remaining cirrus days of the IFO. This difference in thickness is evident in Fig. 15 where the CS data, a subset of the IFO data, are also consistent with the results of PSD. The variation of the CS volume absorption coefficients in Fig. 16 are not as well behaved as emittance and cloud thickness when considered as a function of T_c. Except for the highest and lowest temperatures, though, σ_a for the CS data is close to that observed by PSD. Differences between the IFO and CS data are also seen in the behavior of σ_a suggesting that thickness is not the only discrepancy between the CS and other IFO clouds. Cloud ice water content or phase may also also affect these differences.

The well-correlated variation of r_ϵ suggests the possibility that T_t as well as T_c may be retrieved with VIS-IR radiance pairs. This parameter integrates many of the other parameters examined earlier. Since cloud thickness is small for the highest clouds, there is little difference in T_c and T_t. At lower altitudes, there is more cloud thickness so it is possible to sense radiation from areas deep within the cloud. Whether the relationship shown in Fig. 17 is typical for all observing angles is unknown. From this relationship and those shown in Figs. 15 and 16, it should be possible to obtain reasonable estimates of h and T_t assuming that T_c is determined accurately.

The GOES IR optical depths are consistently less than the AVHRR values by ~ 0.1. This difference indicates the possibility of a calibration offset in the thermal channels. Despite this obvious bias, the good relative agreement in Fig. 20 between the corrected AVHRR emittances and the GOES emittances suggests that (3) is a reasonable approximation to the IR absorption optical depth. Any IR scattering effects which are ignored here are apparently insignificant compared to the other error sources.

b. VIS parameters

Derivation of T_c from a given VIS-IR radiance pair depends critically on the values of τ_v and r. These parameters are subject to the model used in the analysis, the sizes and shapes of the particles in the cloud, and the cloud field geometry. The physical model used for extracting the cloud albedo from the measured reflectance also influences the values of τ_v and r. The fact that there is good agreement between the average derived values of r over land and water at the same hour (i.e., 1600 GMT) suggests that (5) is a reasonable model for accounting for surface reflectance. Thus, other factors are most likely to cause the observed variations in the scattering efficiency.

Theoretically, r approaches a value of 2.0 asymptotically from a maximum of ~ 4 when the size parameter, $2\pi a/\lambda >> 1$ (e.g., Hansen and Travis, 1974).

The scattering wavelength is λ, and a is the particle radius. This theory requires that the IR absorption efficiency is unity and no absorption occurs in the VIS. PSD have presented theoretical results indicating that r is also a function of particle shape. Though there is considerable uncertainty associated with the parameters derived for a given scene, the averaged data presented here for both the CS and IFO scenes are consistent with the limit of $r = 2.0$.

The results shown in Fig. 13 also indicate that r depends on T_c. For $T_c < 235$ K, the average scattering ratio is $\bar{r} = 2.46 \pm 0.20$, while for $T_c > 235$ K, $\bar{r} = 1.85 \pm 0.17$. Some of this difference may be due to temporal sampling differences. The sampling effects may be estimated using the hourly mean values of r in Table 3 to compute $\bar{r}$ instead of the observed values. Using that approach, $\bar{r} = 1.96$ for $T_c > 235$ K and $\bar{r} = 2.09$ for $T_c < 235$ K. The former value is not statistically different from the observed mean scattering ratio for $T_c > 235$ K. The latter value of $\bar{r}$, however, is statistically different from 2.46, indicating that the values of $r > 2.0$ for the lower temperatures are significant. A reanalysis of the data using $\chi_c(r=2.08)$ from Table 6 also yielded temporally unbiased values of $\bar{r}$ for a given T_c. The results using $\chi_c(r=2.08)$ retain the trend of increasing $\bar{r}$ with decreasing T_c (Fig. 23). This reanalysis reveals an almost linear trend of τ_v with h (Fig. 24) lending further support to the potential for deriving cirrus cloud thickness from the VIS-IR data.

Platt and Dilley (1981) found that the lidar-measured backscatter-to-extinction ratio is relatively constant for $T_c > 233$ K. The value of that ratio changes abruptly around 233 K to a new value. Heymsfield and Platt (1984) were able to show that the number density of large particles in cirrus clouds decreased substantially when the temperature dropped below -40°C. Their data also show that ice crystal habits change significantly when the temperature drops below 233 K. A combination of smaller crystals and different shapes may explain the increase in r for $T_c < 235$K observed in the current data set.

The temporal biases in r are primarily due to shortcomings in the analysis' treatment of χ_c. Optical depth and particle shape are two of the more important variables determining the bidirectional reflectance. The average cloud optical depth in the bidirectional reflectance model used here is probably close to 10, while τ_v for the clouds analyzed in this study is generally smaller than 2. Takano and Liou (1989b) indicate that the reflectance anisotropy diminishes with increasing optical depth for scattering by hexagonal columns. This effect may help explain the larger range of $\chi_c(r=2.08)$ compared to the nominal values of χ_c in Table 6.

The nearly monotonic increase of χ_c with θ in Table 6 for both cases is consistent with the scattering phase function for randomly oriented hexagonal columns reported by Takano and Liou (1989a). Since multiple scattering effects tend to smooth out some of the smaller variations found in the single-scattering phase function, a direct correspondence between the phase function and χ_c is not expected. The prominent trends, however, should be apparent for the optical depths considered here. The minimum value of χ_c at $\theta = 120°$ in the afternoon is near the minimum in the phase function of Takano and Liou (1989a), while the distinct maximum near noon corresponds to the backscatter relative maximum in the theoretical model. Mie calculations for a sphere with a 10-μm radius would produce an increase in χ_c with θ between 100° and ~ 135° followed by a flattening of the values of χ_c for greater scattering angles until $\theta > 170°$ where the glory becomes apparent (Hansen and Travis, 1974). These trends suggest that a model which simulates reflected radiances for a cirrus cloud using a phase function for spheres may bias the values of τ_v derived from measurements taken at a given θ.

c. <u>"Dark" pixels</u>

It is possible that the "dark" pixels noted earlier may be caused by the extreme reflectance anisotropy expected for very thin clouds. For small values of τ_v and $\theta \sim 120°$, there should be very little reflection from the cloud in the direction of the satellite compared to its albedo to upwelling diffuse radiation from the surface. Thus, the pixel may appear darker than a clear scene for the same viewing and illumination conditions.

Although such a mechanism may cause some pixel darkening, it is probably not the primary one. Cloud shading is more likely to be the predominant cause of dark pixels. For example, at altitudes of 10 km, a 2-km thick cloud can cast a shadow which has its leading edge removed at least 8-km horizontally on the surface from the position of the cloud's leading edge for $\theta_0 \geq 45°$. Thus, the cloud and the portion of the surface affected by direct transmission through the cloud can easily be offset by one or more

GOES pixels. The projected line of site from the satellite through a cloud will not line up with the cloud's shadow unless $\theta \approx 180°$. In most instances, therefore, the direct transmission from the surface through the viewed cloud will come from the shadow of a different cloud. The diffuse reflectance will result from the combined effects of the various clouds in the vicinity. For a homogeneous cloud field, an optically thick viewed cloud, or $\theta = 180°$, such effects are negligible. Figures 1, 2, and 21 provide ample evidence that the clouds observed during the CS are neither optically thick nor homogeneous. In an inhomogeneous cloud field, it is possible to observe a surface darkened by the shadow of a thick cloud through a thin cloud which produces little scattering of its own in the direction of the satellite. Thus, to the viewer in space a pixel appears to be a cloud by virtue of its cold temperature, but is darker than expected for a clear scene.

This effect may be examined quantitatively by considering (5). Use of that model implicitly assumes a homogeneous cloud field. To consider an inhomogeneous cloud field, let τ_s replace τ_v in (6), where τ_s is the VIS optical depth of the cloud casting a shadow onto the surface in the line of site of the observed cloud which has optical depth τ_v. Since the diffuse radiation emerging from the bottom of the clouds and reflecting from the surface is coming from all of the clouds in the field, let α_c in the third term of (5) be replaced by the average albedo of the observed and the shading cloud. The results of solving this inhomogeneous version of (5) for two different observed clouds are displayed in Fig. 25. The circles represent $\tau_s = \tau_v$. Viewing angles were fixed at $\theta = 52°$ and χ_c varied with θ_0 as in the lower half of Table 3. Clear-sky reflectance is denoted with the dashed horizontal line.

The greatest effects of cloud inhomogeneities are seen for $\tau_v = 0.25$. Both shading clouds cause dark pixels for $\theta_0 < 81°$. Some dark pixels occur for $\tau_s = \tau_v$ for $\theta_0 < 60°$. Calculations using smaller μ_0's produced no dark pixels. The thickness of the shading cloud becomes more important as μ_0 increases. The impact of shading on the observed cloud having $\tau_v = 1$ is less pronounced with little likelihood of dark pixels for the range of μ_0 considered. Shading by the thin cloud ($\tau_s = 0.25$) actually increases the observed reflectance for all cases using $\tau_v = 1$. As τ_v increases to larger values, the impact of τ_s will become negligible. This lack of shadowing effect for larger clouds suggests that the observed reflectance may be biased toward a value which is lower than expected when the scene contains both optically thick ($\tau_v \geq 2$) and thin clouds, even if no dark pixels occur.

Shadowing effects can be observed in the data shown in Fig. 22. Dark pixels corresponding to the thinnest part of the cloud are seen before 2027 GMT. The next few pixels to the right are detectable but τ_v is much less than τ_e. The VIS optical depth for the pixels corresponding 2040 GMT is more than three times the value of τ_e suggesting enhanced reflectance. In this figure, the sun would be located approximately to the right of the figure at $\theta_0 = 68°$. With a cloud top near 11 km, the thickest part of the cloud would cast a shadow approximately 28 km to the left or to the position corresponding to 2025 GMT. The view from the satellite is at a 35° angle, not perpendicular, to the solar plane. Thus, the surface in the line of site of the cloud at 2025 GMT would correspond to the 2020 GMT position. That surface would be shaded by a cloud with $\tau_e \approx 0.5$ or $\tau_v \approx 1.0$ assuming that Fig. 22 is an accurate cross-section of the cloud. A dark pixel would be expected at 2020 GMT based on the results in Fig. 25. The first visibly detectable cloud coincides with $\tau_e \approx 0.3$ at 2027 GMT. Its value of τ_v is much less than the expected value of 0.6.

While the shading can explain the darker pixels, it does not account for the excessively bright ones at 2040 GMT. For these bright pixels, it is instructive to refer to the cloud structure in Fig. 1. The vertical thickness of the cloud changes rapidly so that the pathlength of the incident solar radiation through the cloud is not necessarily $h\sec\theta_0$. The pathlength may be substantially increased because of the cloud structure. For example, the sun angle may coincide with the right arm of the "V" defining the cloud centered at 2035 GMT in Fig. 1. This effect would tend to cause a cloud to appear brighter than expected for the observed τ_e. In this case, the shadowing and enhancement effects apparently cancel to yield a reasonable value of r for the whole scene.

The occurrence of dark pixels is shown in Fig. 26 as a function of ϵ_b. Most of the dark pixels are found at emittances corresponding to $\tau_e < 0.2$. Some, however, are found for $\tau_e = 0.5$. Very few dark pixels were observed near noon when $\theta > 160°$. Most were found in the midmorning and late afternoon when shading conditions were favorable. The dark pixels comprise only 3% of the data considered here. This percentage belies the importance of this effect since shading will occur in many instances without producing the easily detectable dark pixels. The shading effect will tend to reduce the observed reflectance causing an underestimation of the cloud's thickness and emittance. Cloud shadows or their absence will also affect the interpretation of reflectance anisotropy. Their presence at high solar zenith angles will yield lower than normal values of τ_v.

6. Concluding Remarks

The cirrus clouds observed during the case study days are similar to those observed in previous research. By comparison, however, they are not necessarily typical of midlatitude cirrus clouds since their bulk properties are significantly different from those observed during other IFO cirrus days.

The analysis performed in this study using a combination of ground-based and satellite instrumentation yielded some results which are similar to earlier studies using other combinations of platforms and instruments. This consistency of results for different approaches lends a higher degree of confidence to the common findings. In addition, the combined data sets used here have provided some valuable new insight into the problem of determining cirrus cloud properties using VIS and IR radiance pairs from satellites.

The determination of cloud-top emittance or actual cloud-top temperature appears to be feasible based on the results of this study. Previously, what has been termed cloud-top temperature in emittance-adjusted VIS-IR retrievals is closer to to cloud center temperature. The emittance ratio and the dependency of cloud thickness on cloud-center temperature derived here may be utilized in a scheme to estimate cloud thickness. This latter parameter will be useful for computing radiative divergence for observed cirrus clouds.

The results indicate that scattering efficiencies are greater for colder clouds. This finding holds promise for improvements in determining the IR optical depth from reflected VIS data. Additional study, however, is required to confirm this conclusion.

From the examination of the reflectance data and scattering efficiencies it is concluded that much work remains to adequately describe the scattered radiation field for real cirrus clouds. Both theoretical and empirical bidirectional reflectance models should be developed for clouds composed of realistic particle shapes. As in the ISCCP model, the patterns should be developed for various optical depths. Those models will require confirmation with the aid of further observational data. The effects of cloud particle scattering in IR radiative transfer should also be examined observationally.

Cloud shadows are a problem for the interpretation of cloud reflectances, especially for cirrus. The effects are not limited to large solar zenith angles. Relatively high viewing zenith angles can produce situations which cause the viewing of shadows even for the near-zenith sun. It is apparent that analysis of a single pixel is most subject to shadowing problems. Some of the effects may be diminished through averaging over several pixels. Other approaches to dealing with shading need to be developed. Validations of cirrus scattering calculations must also consider these effects. The problem of shadows is not as important over water because of the low surface albedo. Other problems in remote sensing of clouds such as partially cloud-filled pixels have not been considered here. Future research efforts should address these other factors.

Acknowledgements

The contributions of Messrs. P. Heck, R. Wheeler, and G. Gibson of Planning Research Corporation to the satellite data reduction and graphics are deeply appreciated. We also thank Ms. S. Morgan of Computer Sciences Corporation for her assistance in reducing the GOES data. Discussions with Dr. B. Wielicki of NASA Langley Research Center and Prof. K-N. Liou of the University of Utah were also quite helpful. The Madison lidar measurements were supported by ARO grant DAAG29-84-K-0069, ONR grant N00014-87-K-0436, and NASA grant NAAG1-882.

APPENDIX

List of Symbols

a	particle radius
B	Planck function at 11.5 μm
D, D_s	observed and clear-sky visible counts
h	cloud thickness
k, k_0	albedo coefficient, ozone absorption coefficient
k_{max}	albedo coefficient for maximum high-cloud albedo
r, r_ϵ	scattering efficiency ratio, cloud-top/-center emittance ratio
T, T_s	observed and clear-sky 11.5 μm equivalent blackbody temperatures
T_c, T_t	cloud-center and -top 11.5 μm equivalent blackbody temperatures
T_a, T_{cs}	clear-sky temperatures estimated from surface and satellite data
T_z, T_g	air temperatures at altitude z and at the surface
T_{max}	maximum observed 11.5 μm equivalent blackbody temperature
t	time
u	ozone abundance
z_b, z_c, z_t	cloud-base, cloud-center, and cloud-top altitudes
α_c, α_d	cloud and diffuse cloud albedos
α_s, α_{sd}	clear-sky albedo, clear-sky diffuse albedo
α_{max}	maximum albedo for high clouds at a given emittance
β_π	volume backscatter coefficient
ϵ_a, ϵ_b	vertical effective emittance, effective beam emittance
θ	single-scattering angle

θ, θ_0	viewing zenith angle, solar zenith angle
λ	latitude or wavelength
μ, μ_0	$\cos\theta$, $\cos\theta_0$
ρ, ρ_s, ρ_c	observed, clear-sky, and cloud visible reflectance
σ_a	volume extinction coefficient
τ_e, τ_v	infrared absorption and visible scattering optical depths
τ_s	visible scattering optical depth of shading cloud
T_a, T_c, T_u	ozone, downward cloud, and upward cloud transmittances
ϕ	longitude
χ_s, χ_c	clear-sky and cloud anisotropic reflectance factors
ψ	relative azimuth angle
CS	Case Study (October 27-28, 1986)
IFO	Intensive Field Observations (October 19 - November 2, 1986)
IR	infrared (11.5 μm)
FMC	Ft. McCoy, Wisconsin
GMT	Greenwich Mean Time
MAD	Madison, Wisconsin
WAU	Wausau, Wisconsin
VIS	visible (0.65 μm)

REFERENCES

Alvarez, J. M., J. G. Moore, and M. A. Vaughn, 1989: The 27-28 October 1986 FIRE IFO cirrus case study: A dual-polarization lidar view from Ft. McCoy, Wisconsin. Mon. Wea. Rev., this issue.

Grund, C. J., and E. W. Eloranta, 1989: The 27-28 October 1986 FIRE IFO cirrus case study: Optical properties of cirrus clouds measured by the high spectral resolution lidar. Mon. Wea. Rev., this issue.

Hahn, C. J., S. G. Warren, and J. London, 1988: Surface synoptic cloud reports for Wisconsin, 86 Oct - Nov 3. Cooperative Inst. for Research in Environ. Sci., Campus Box 449, Univ. of Colo., Boulder, 80309, 15 pp.

Hansen, J. E. and L. D. Travis, 1974: Light scattering in planetary atmospheres. Space Sci. Rev., **16**, 527-610.

Heymsfield, A. J., and C. M. R. Platt, 1984: A parameterization of the particle size spectrum of ice clouds in terms of the ambient temperature and the ice water content. J. Atmos. Sci., **41**, 846-855.

Liou, K. N., 1973: Transfer of solar irradiance through cirrus cloud layers. J. Geophys. Res., **78**, 1409-1418.

--------, 1986: Influence of cirrus clouds on weather and climate processes: A global perspective. Mon. Wea. Rev., **114**, 1167-1199.

--------, and G. D. Wittman, 1979: Parameterization of the radiative properties of clouds. J. Atmos. Sci., **36**, 1261-1273.

McClatchey, R. A., R. W. Fenn, J. E. A. Selby, F. E. Volz, and J. S. Garing, 1973: Optical properties of the atmosphere (3rd edition). AFCGRL-72-0497, ERP No. 411, 113 pp.

Minnis, P., and E. F. Harrison, 1984a: Diurnal variability of regional cloud and clear-sky radiative parameters derived from GOES data, Part I: Analysis method. J. Clim. Appl. Meteor., **23**, 993-1011.

---------, and -------------, 1984b: Diurnal variability of regional cloud and clear-sky radiative parameters derived from GOES data, Part III: November 1978 radiative parameters. J. Clim. Appl. Meteor., **23**, 1032-1051.

---------, E. F. Harrison and G. G. Gibson, 1987: Cloud cover over the eastern equatorial Pacific derived from July 1983 ISCCP data using a hybrid bispectral threshold method. J. Geophys. Res., **92**, 4051-4073.

----------, P. W. Heck, and E. F. Harrison, 1989: The 27-28 October 1986 FIRE Cirrus IFO case study: Cloud parameter fields derived from satellite data. Mon. Wea. Rev., this issue.

Paltridge, G. W., and C. M. R. Platt, 1981: Aircraft measurements of solar and infrared radiation and the microphysics of cirrus cloud. Quart. J. Roy. Meteor. Soc., **107**, 367-380.

Platt, C. M. R., 1973: Lidar and radiometric observations of cirrus clouds. J. Atmos. Sci., **30**, 1191-1204.

--------------, 1979: Remote sounding of high clouds, I: Calculations of visible and infrared optical properties from lidar and radiometer measurements. J. Appl. Meteor., **18**, 1130-1143.

--------------, 1983: On the bispectral method for cloud parameter determination from satellite VISSR data: Separating broken cloud and semitransparent cloud. J. Clim. Appl. Meteor., **22**, 429-439.

--------------, and A. C. Dilley, 1979: Remote sounding of high clouds: II. Emissivity of cirrostratus. J. Appl. Meteor., **18**, 1144-1150.

--------------, and A. C. Dilley, 1981: Remote sounding of high clouds: IV. Observed temperature variations in cirrus optical properties. J. Atmos. Sci., **38**, 1069-1082.

-------------, and -----------, 1984: Determination of cirrus particle single-scattering phase function from lidar and solar radiometric data. Appl. Opt., **23**, 380-386.

-------------, and G. L. Stephens, 1980: The interpretation of remotely sensed high cloud emittances. J. Atmos. Sci., **37**, 2314-2322.

-------------, D. W. Reynolds and N. L. Abshire, 1980: Satellite and lidar observations of the albedo, emittance and optical depth of cirrus compared to model calculations. Mon. Wea. Rev., **108**, 195-204.

-------------, J. C. Scott, and A. C. Dilley, 1987: Remote sounding of high clouds, VI. Optical properties of midlatitude and tropical cirrus. J. Atmos. Sci., **44**, 729-747.

Reynolds, D. W., and T. H. Vonder Haar, 1977: A bispectral method for cloud parameter determination. Mon. Wea. Rev., **105**, 446-457.

Rossow, W. B., L. C. Garder, P. Lu and A. Walker, 1988: International Satellite Cloud Climatology Project (ISCCP), Documentation of cloud data. WCRP Report, August, 78 pp.

Sassen, K., C. J. Grund, J. Spinhirne, M. Hardesty, and J. M. Alvarez, 1989: The 27-28 October 1986 FIRE IFO cirrus case study: A five lidar view of cirrus cloud structure and evaluation. Submitted to Mon. Wea. Rev.

Shenk, W. E., and R. J. Curran, 1973: A multispectral method for estimating cirrus cloud top heights. J. Appl. Meteor., **12**, 1213-1216.

Schiffer, R. A., and W. B. Rossow, 1983: The International Satellite Cloud Climatology Project (ISCCP): The first project of the World Climate Research Progamme. Bull. Am. Meteorol. Soc., 64, 779-784.

Spinhirne, J. D., D. L. Hlavka and W. D. Hart, 1988: ER-2 lidar observations from the October 1986 FIRE cirrus experiment. NASA TM 100704, 49 pp.

Starr, D. O'C., 1987: A cirrus-cloud experiment: Intensive Field Observations planned for FIRE. Bull. Am. Meteor. Soc., **68**, 119-124.

Stephens, G. L., 1980: Radiative properties of cirrus clouds in the infrared region. J. Atmos. Sci., **37**, 435-446.

Stuhlmann, R., P. Minnis and G. L. Smith, 1985: Cloud bidirectional reflectance functions: a comparison of experimental and theoretical results. Appl. Opt., **24**, 396-401.

Suttles, J. T., R. N. Green, P. Minnis, G. L. Smith, W. F. Staylor, B. A. Wielicki, I. J. Walker, D. F. Young, V. R. Taylor and L. L. Stowe, 1988: Angular radiation models for Earth-atmosphere system: Volume I - Shortwave radiation. NASA RP 1184, 144 pp.

Takano, Y. and K. N. Liou, 1989a: Radiative transfer in cirrus clouds: I. Single scattering and optical properties of oriented hexagonal ice crystals. J. Atmos. Sci., **46**, 3-20.

-------- and -------, 1989b: Radiative transfer in cirrus clouds: II. Theory and computation of multiple scattering in an anisotropic medium. J. Atmos. Sci., **46**, 21-38.

Whitlock, C. H., L. Poole, J. Alvarez, D. Robinson, C. Grund, K. Sassen, D. Starr, S. Cox, S. LeCroy, R. Frouin, and G. Smith, 1989: Cirrus cloud fraction and optical depth from surface observations during the Wisconsin FIRE/SRB experiment. Mon. Wea. Rev., this issue.

Table 1. Times and locations of lidar-satellite data used in this study.

Site	Month	Day	Times (GMT)
FMC	October	22	1300, 1330, 1400, 1600, 1630, 1700, 2000
		27	2030, 2100
		28	1330, 1400, 1430, 1500, 1600, 1700, 1900 1930, 2000, 2030, 2100, 2130, 2200
		30	2000, 2030
	November	1	1800, 1900
		2	1900, 2000, 2100
MAD	October	28	1330, 1500, 1600, 1700, 1800, 1930, 2000 2030, 2100, 2130, 2200
WAU	October	22	1300, 1330, 1400, 1430, 1600, 1630, 1700, 1800 1830, 1900, 1930, 2130, 2200
		28	1500, 1600, 1700, 1800, 1900, 1930, 2000, 2030 2100, 2130
		30	2130, 2200
	November	1	1800, 1900, 2000
		2	1700, 1800, 1900, 2000, 2100

Table 2. Observed and computed cloud properties for October 1986 Case Study.

Site (Day)	GMT	T_s (K)	z_t (km)	h (km)	T_c (K)	T_t (K)	τ_e	τ_v	dark pixel %
FMC									
(27)	2030	287.7	9.6	1.1	227.8	225.1	0.11	0.24	4
	2100	286.9	10.3	1.6	228.7	220.3	0.19	0.48	0
(28)	1330	278.3	9.5	2.1	237.9	227.7	0.22	0.12	0
	1400	279.7	11.0	1.3	231.6	216.8	0.14	0.17	5
	1430	280.5	11.2	1.5	230.0	215.6	0.18	0.31	11
	1500	281.6	10.1	1.3	239.4	222.5	0.31	0.59	7
	1600	283.0	10.0	3.0	240.1	223.2	0.80	1.72	0
	1700	287.9	10.4	1.9	223.0	219.6	0.23	0.90	0
	1900	285.4	10.8	2.1	227.5	217.1	0.23	0.57	0
	1930	285.5	10.9	2.6	228.9	216.6	0.41	0.93	3
	2000	285.9	11.0	1.9	224.4	216.3	0.41	1.03	0
	2030	284.8	10.9	1.7	220.7	216.4	0.62	1.75	6
	2100	280.9	10.7	2.4	230.7	216.7	0.79	1.42	5
	2130	281.2	10.8	2.2	226.3	216.4	0.44	0.73	11
	2200	276.8	10.9	2.4	221.7	216.1	0.32	0.28	0
MAD									
(28)	1330	278.4	10.8	3.4	237.9	217.9	0.16	0.18	3
	1500	280.2	10.8	4.2	242.8	217.7	0.24	0.63	2
	1600	281.7	10.6	3.7	241.9	218.5	0.58	1.10	0
	1700	284.8	10.5	4.3	240.4	218.8	0.40	0.89	0
	1800	289.1	9.8	3.2	229.4	224.6	0.14	0.89	0
	1930	287.7	10.7	1.8	222.1	217.3	0.10	0.30	3
	2000	286.5	10.7	1.8	221.7	217.1	0.10	0.46	7
	2030	286.6	10.7	3.1	223.3	217.1	0.34	0.84	3
	2100	286.0	10.5	2.4	223.3	217.2	0.29	0.53	33
	2130	284.5	10.8	4.0	232.2	216.4	0.55	0.42	3
	2200	281.1	10.5	4.2	237.4	216.8	0.44	0.27	13
WAU									
(28)	1500	279.0	9.8	3.2	238.0	225.0	1.67	3.17	0
	1600	282.5	10.1	3.1	238.0	222.4	1.40	2.33	0
	1700	287.1	10.1	3.9	235.0	222.3	1.21	2.38	0
	1800	288.4	10.3	4.1	231.0	220.3	1.13	3.00	0
	1900	285.7	11.0	0.8	217.1	216.4	0.19	0.69	0
	1930	283.9	10.9	2.1	226.4	216.6	0.30	1.00	0
	2000	284.4	10.9	2.9	236.1	216.5	1.04	2.35	0
	2030	285.4	10.7	3.1	231.0	216.9	1.34	3.69	0
	2100	284.1	10.6	3.2	234.0	217.0	0.36	1.43	7
	2130	279.7	11.0	1.0	217.0	216.0	0.29	0.44	1

Table 3. Reflectance parameters computed for all data.

GMT	Cases (IFO)	θ (°)	ψ (°)	Θ (°)	All Data (IFO)		Case Study	
					τ_v	r	τ_v	r
1330	4	80.2	106.6	109	0.97	1.08	0.15	0.85
1400	3	75.6	112.6	117	1.84	1.42	0.17	1.19
1430	2	71.3	118.6	124	0.90	1.76	0.31	1.68
1500	3	67.9	125.7	131	1.46	2.01	1.46	2.01
1600	5	61.0	140.0	146	2.31	2.22	1.72	1.98
1630	2	57.8	147.7	153	2.44	1.74	----	----
1700	6	57.6	156.6	160	1.78	2.99	1.39	2.94
1800	6	57.3	174.1	173	2.20	3.49	1.94	5.65
1830	1	56.1	177.1	175	3.52	1.98	----	----
1900	7	59.9	169.0	168	2.50	2.81	0.63	3.13
1930	4	61.1	160.8	162	1.52	2.73	0.74	2.76
2000	8	65.0	153.6	154	1.93	2.68	1.28	3.06
2030	5	68.3	146.5	147	1.40	2.47	1.63	2.34
2100	6	72.8	140.3	140	1.06	1.99	0.97	2.46
2130	4	76.2	133.6	132	1.15	1.30	0.53	1.20
2200	5	81.2	128.1	125	0.67	0.83	0.28	0.68
totals and means	71	67.2	145.4	---	1.69	2.08	1.04	2.07

Table 4. Observed and computed cloud properties for Case Study ER-2 data.

Day	GMT	Lat. (°N)	Lon. (°W)	T_s (K)	T_c (K)	h (km)	τ_e	τ_v	r	dark pixel %
27	1830	45.8	93.1	290.0	225.0	0.5	0.12	0.69	5.73	0
	1900	45.3	92.5	288.5	234.0	0.5	0.14	0.51	3.43	0
	1930	44.9	91.1	281.0	234.0	0.5	0.24	0.73	2.91	3
28	1600	44.6	87.0	283.0	229.0	3.7	0.43	0.86	1.99	0
	1600	44.5	87.1	283.0	229.0	3.7	0.42	0.92	2.12	0
	1600	44.5	87.1	283.0	229.0	3.7	0.45	1.00	2.21	0
	1800	43.6	89.4	281.0	228.0	1.5	0.29	0.90	3.23	0

Table 5. Comparison of AVHRR- and GOES-derived cloud parameters.

Site (Day)	T_c (K)	AVHRR Parameters						GOES Parameters				
		GMT	θ (°)	τ_e	τ_v	r	dark pixel %	GMT	τ_e	τ_v	r	dark pixel %
FMC												
(28)	231	2100	141	0.83	1.49	1.92	0	2100	0.72	1.36	1.77	3
(30)	223	2042	127	0.25	0.34	1.13	18	2030	0.17	0.60	3.29	3
(2)	230	2006	92	0.49	1.15	1.88	5	2000	0.39	0.93	2.32	0
WAU												
(28)	234	2100	142	0.31	1.72	3.45	0	2100	0.26	0.78	2.15	6
(2)	230	2006	98	1.34	4.61	3.19	0	2000	1.16	3.20	2.67	0

Table 6. Anisotropic reflectance factor comparison.

GMT	Pixels	χ_c (nominal)	χ_c (r=2.08)	mean difference	rms difference
1330	213	0.823	0.620	0.203	0.228
1400	177	0.864	0.745	0.119	0.129
1430	113	0.896	0.895	0.001	0.113
1500	177	0.922	0.876	0.056	0.097
1600	215	0.980	1.023	-0.043	0.130
1630	146	1.002	0.899	0.103	0.112
1700	212	1.020	1.173	-0.153	0.305
1800	158	1.050	1.250	-0.200	0.401
1830	72	1.061	1.133	-0.072	0.125
1900	262	1.029	1.253	-0.224	0.314
1930	236	1.008	1.287	-0.279	0.347
2000	245	0.982	1.110	-0.128	0.208
2030	290	0.953	1.028	-0.075	0.121
2100	222	0.918	0.908	0.010	0.094
2130	283	0.882	0.789	0.093	0.180
2200	210	0.843	0.588	0.255	0.268

FIGURE CAPTIONS

Fig. 1. Outline of cirrus cloud derived from lidar backscatter intensities over FMC, October 28, 1986.

Fig. 2. Estimated lidar volume extinction efficiency from cirrus cloud over WAU, October 28, 1986.

Fig. 3. Comparison of clear-sky and shelter air temperatures over FMC, October 27, 1986.

Fig. 4a. Theoretical observed VIS reflectance over WAU for 1400 GMT ($\rho_s = 0.13$) and for 1800 GMT ($\rho_s = 0.16$).

Fig. 4b. Theoretical observed albedos for various surface albedos.

Fig. 5. Example of low-cloud filter application over FMC at 1930 GMT, October 28, 1986.

Fig. 6a. Clear histogram over FMC at 1500 GMT, October 27, 1986 (numbers denote frequency of occurrence of temperature-count pairs).

Fig. 6b. Histogram of cirrus clouds over FMC at 1500 GMT, October 28, 1986.

Fig. 7a. Cloud emittances and observed reflectances for $T < T_s - 3$ K derived from Fig. 6b.

Fig. 7b. Cloud emittances and cloud albedos derived from Fig. 6b without "dark" pixels.

Fig. 7c. Average cloud emittance as a function of cloud albedo derived from Fig. 7b.

Fig. 8. Average cloud emittance versus cloud albedo at 1500 GMT, October 28, 1986 over three sites.

Fig. 9. Average cloud emittance and albedo at three times during October 28, 1986 over FMC.

Fig. 10. Average cloud emittances and albedos at 2100 GMT over FMC during different days.

Fig. 11a. Average cloud emittance versus cloud albedo for all case study scenes, $T_z = T_c$.

Fig. 11b. Same as Fig. 11b, except for all IFO scenes.

Fig. 12. Variation of mean scattering efficiency with IR optical depth.

Fig. 13. Mean scattering efficiency versus cloud-center temperature.

Fig. 14. Variation of cloud vertical beam emittance with cloud-center temperature.

Fig. 15. Dependence of cloud thickness on cloud-center temperature.

Fig. 16. Cirrus volume absorption coefficient versus cloud-center temperature.

Fig. 17. Same as Fig. 11b, except $T_z = T_c$.

Fig. 18. Dependence of ratio of cloud-top emittance to cloud-center emittance on cloud-center temperature.

Fig. 19. Comparison of cloud albedos and emittances derived from October 28, 1986 GOES and AVHRR data taken at ~ 2100 GMT over WAU.

Fig. 20. Same as Fig. 19, except for November 2, 1986 at ~ 2000 GMT.

Fig. 21. Comparison of GOES and lidar observations along wind vector over FMC during October 28, 1986.

Fig. 22. Cloud optical properties derived from Fig. 21.

Fig. 23. Same as Fig. 13, except for $\chi_c(r=2.08)$.

Fig. 24. Variation of cloud thickness with VIS optical depth for $\chi_c(r=2.08)$.

Fig. 25. Effect of cloud shading on observed reflectance. Solid symbols, $\tau_v = 1$. Open symbols, $\tau_v = 0.25$.

Fig. 26. Percentage of total number of "dark" pixels as a function of effective beam emittance, ϵ_b.

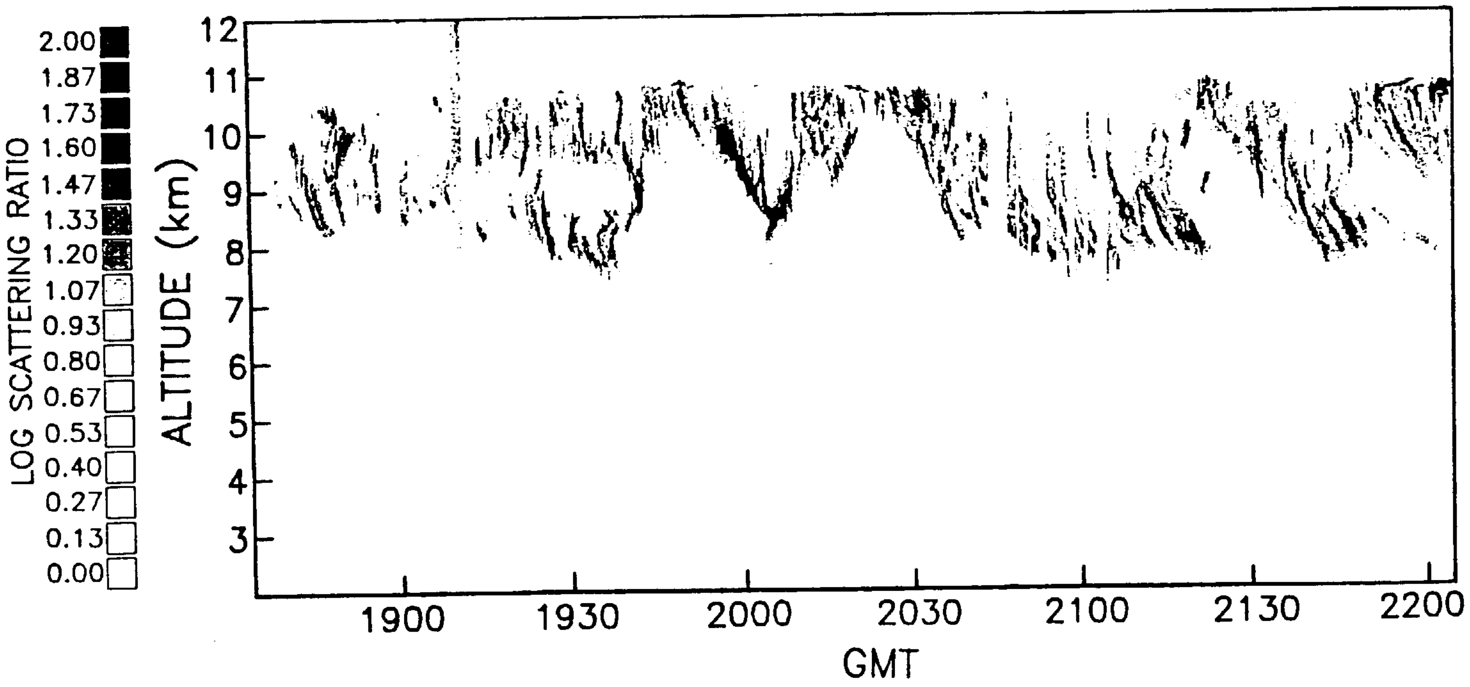
LOG SCATTERING RATIO
2.00
1.87
1.73
1.60
1.47
1.33
1.20
1.07
0.93
0.80
0.67
0.53
0.40
0.27
0.13
0.00
ALTITUDE (km)
12
11
10
9
8
7
6
5
4
3
1900
1930
2000
2030
2100
2130
2200
GMT

Fig. 1

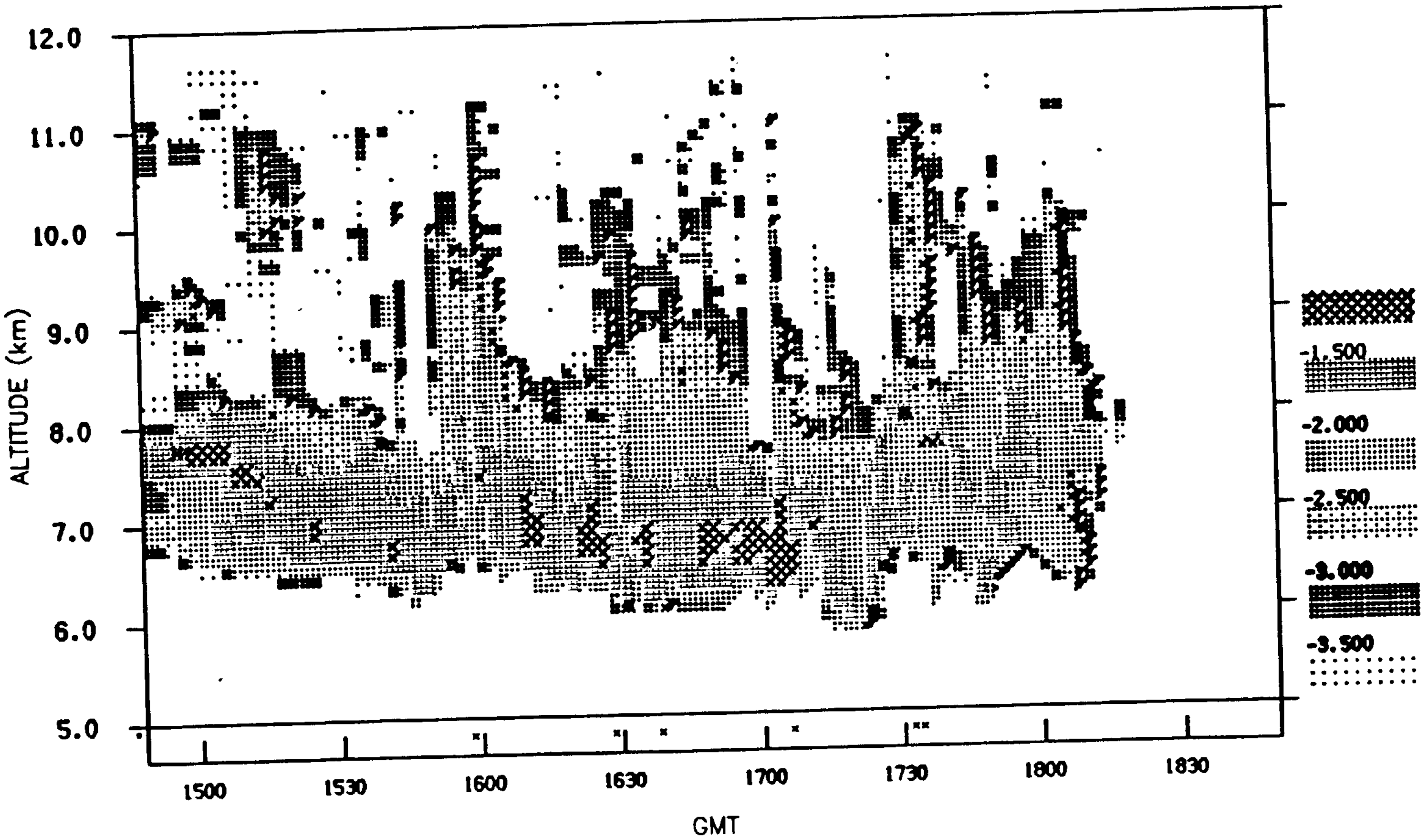

12.0
11.0
10.0
9.0
8.0
7.0
6.0
5.0
ALTITUDE (km)
1500
1530
1600
1630
1700
1730
1800
1830
GMT
-1.500
-2.000
-2.500
-3.000
-3.500

FiG. 2

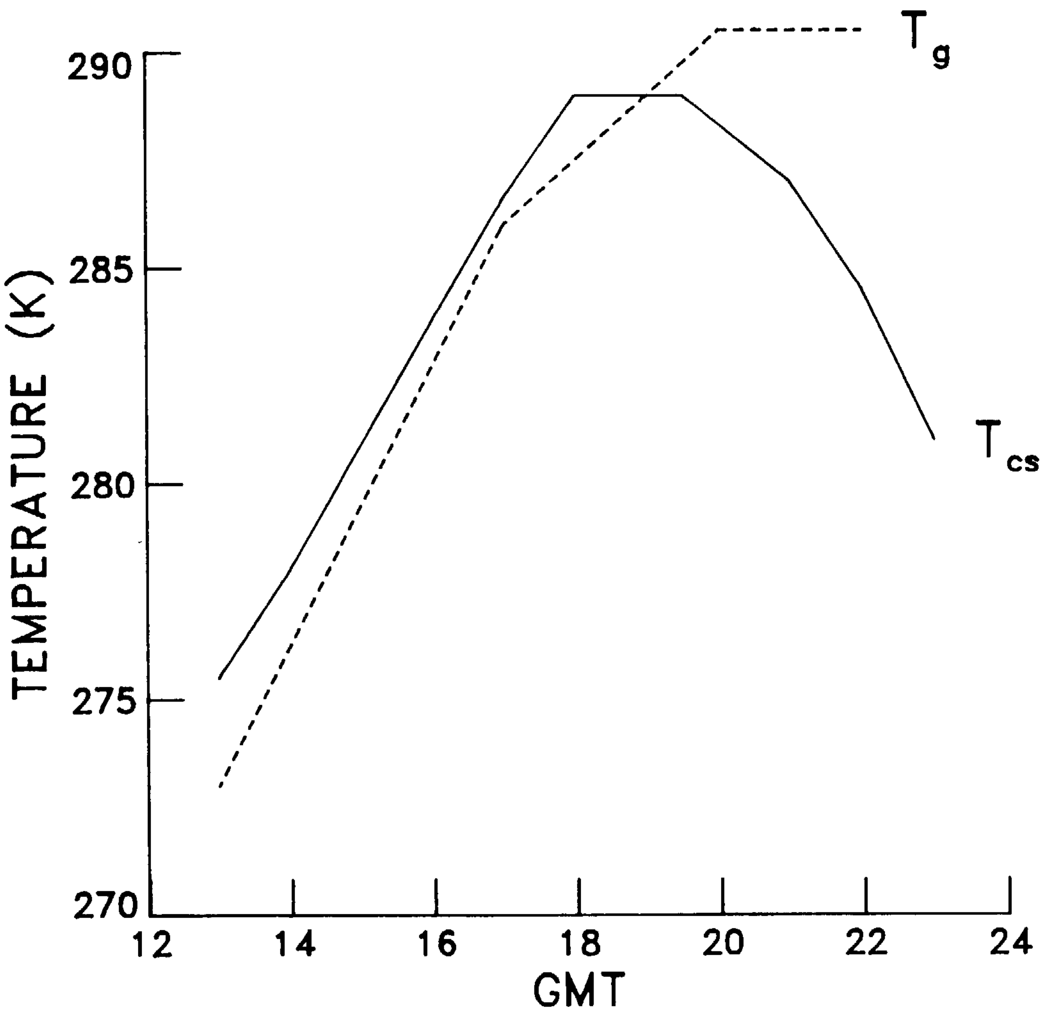

FIG. 3

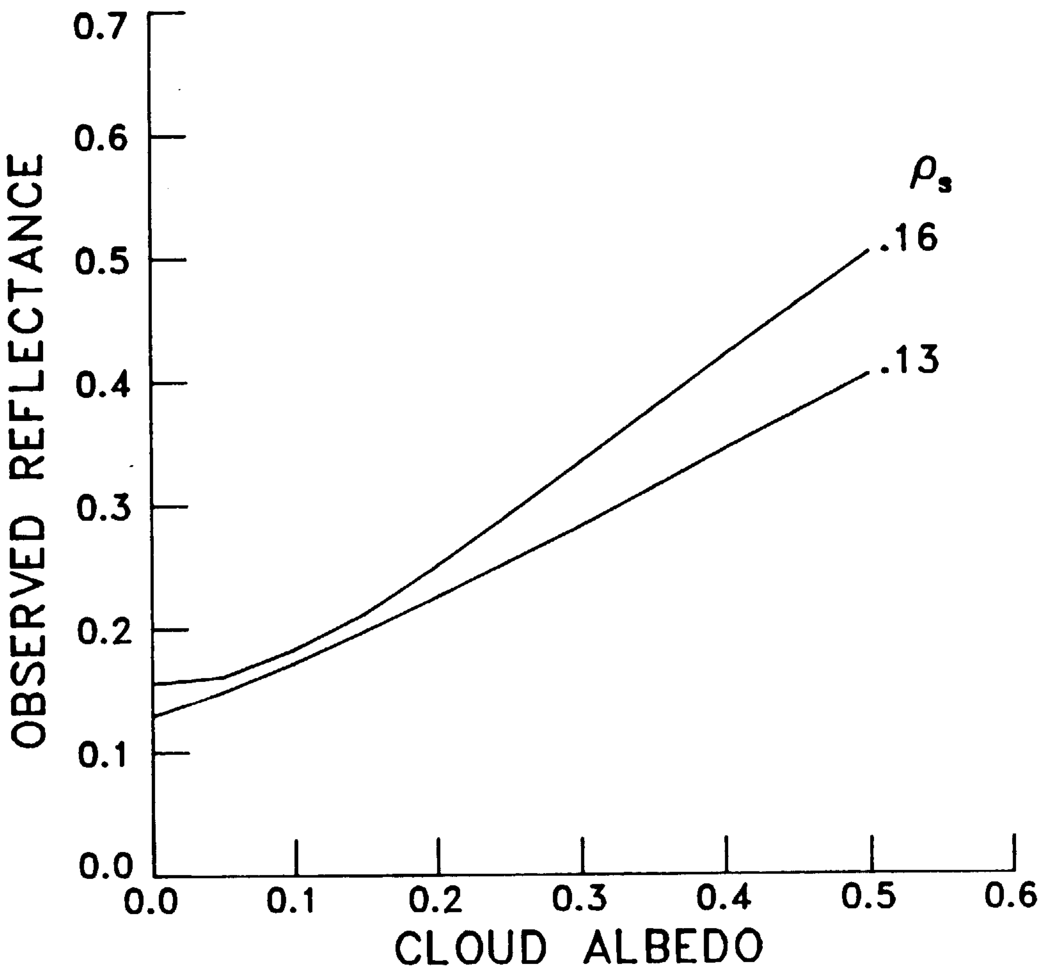
0.7
0.6
0.5
0.4
0.3
0.2
0.1
0.0
OBSERVED REFLECTANCE
ρ_s
.16
.13
0.0
0.1
0.2
0.3
0.4
0.5
0.6
CLOUD ALBEDO

Fig, 4a

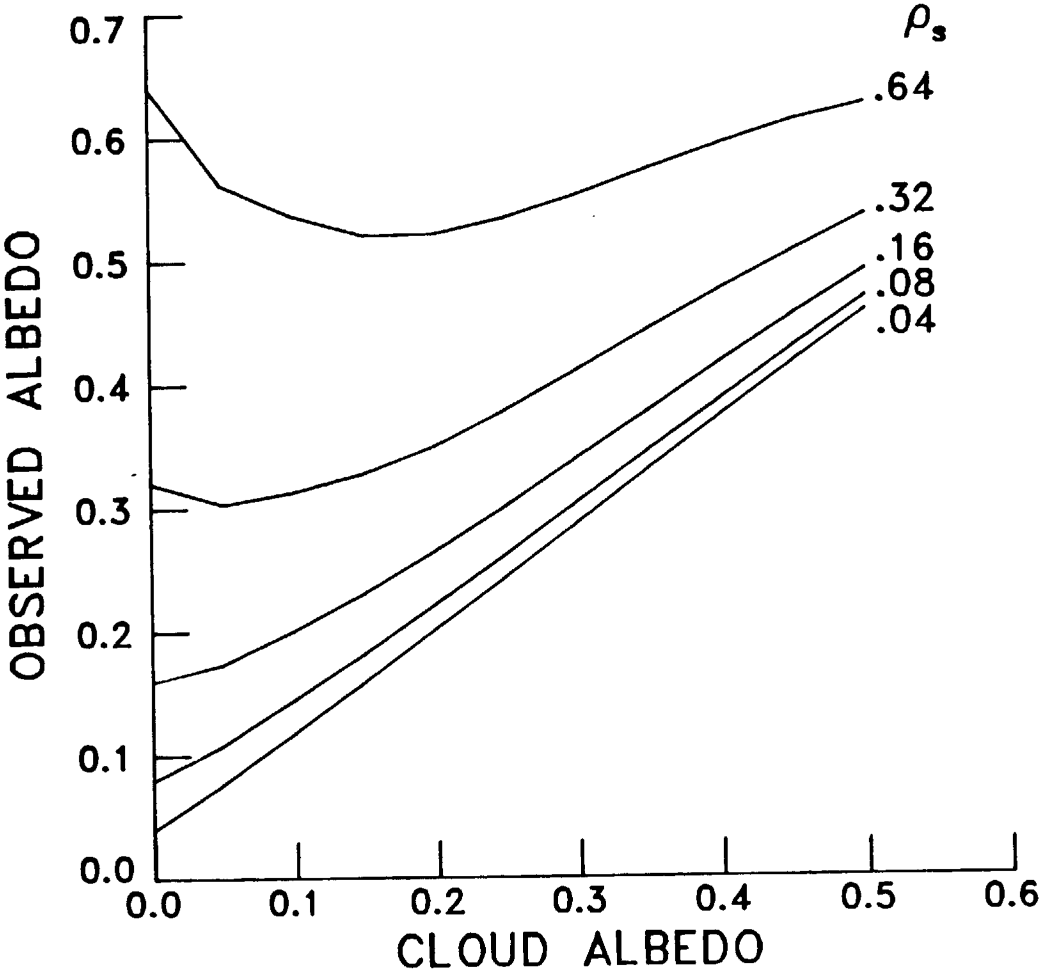

0.7
0.6
0.5
0.4
0.3
0.2
0.1
0.0
OBSERVED ALBEDO
0.0
0.1
0.2
0.3
0.4
0.5
0.6
CLOUD ALBEDO
ρ_s
.64
.32
.16
.08
.04

Fig. 4b

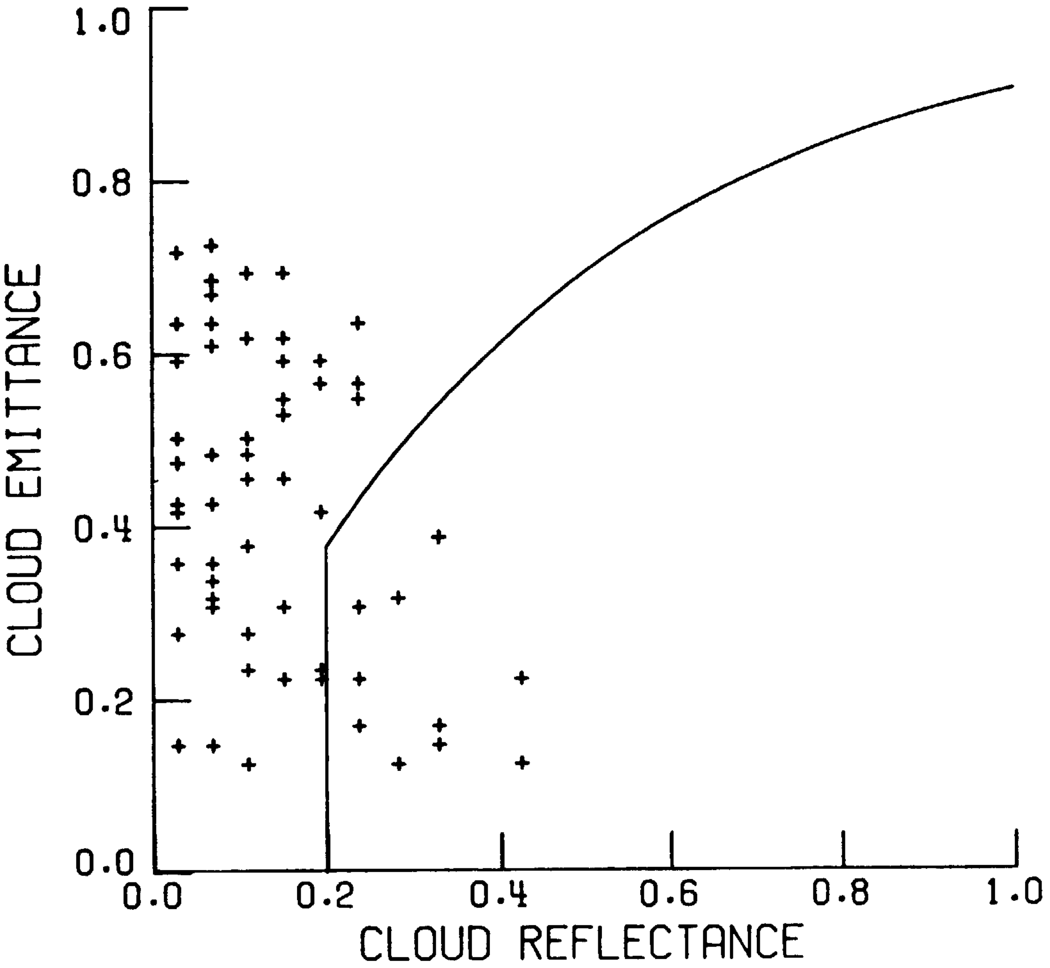
1.0
0.8
0.6
0.4
0.2
0.0
CLOUD EMITTANCE
0.0
0.2
0.4
0.6
0.8
1.0
CLOUD REFLECTANCE

Fig. 5

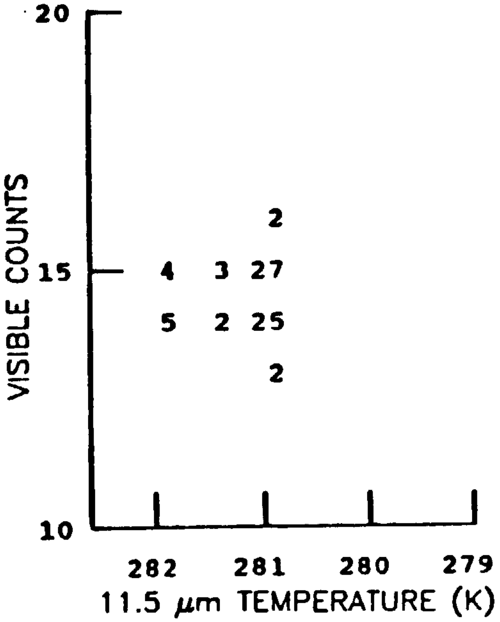
20
15
10
VISIBLE COUNTS
2
4
3
27
5
2
25
2
282
281
280
279
11.5 μm TEMPERATURE (K)

Fig. 6a

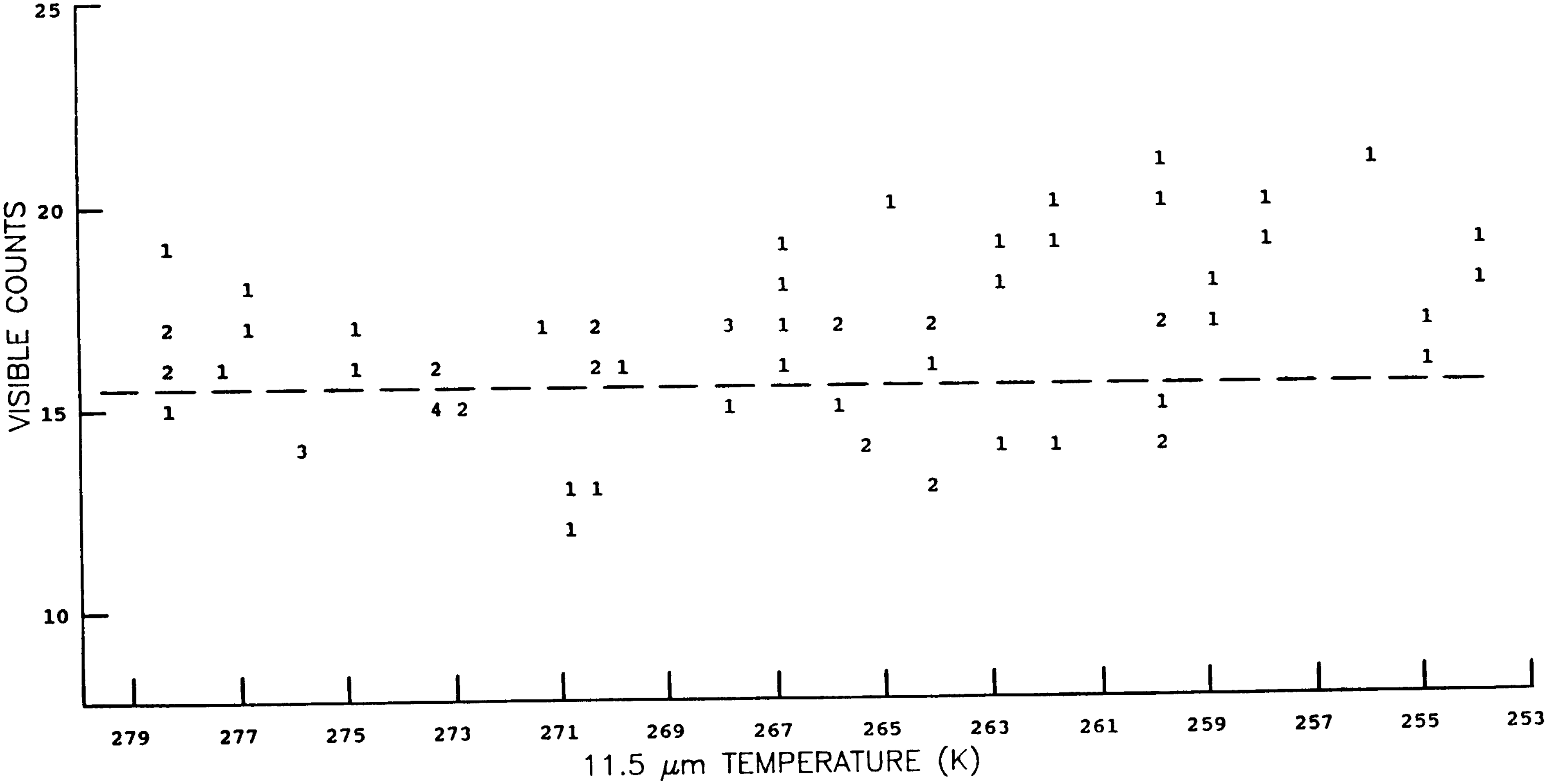

25
20
15
10
VISIBLE COUNTS
279
277
275
273
271
269
267
265
263
261
259
257
255
253
11.5 μm TEMPERATURE (K)

Fig. 6b

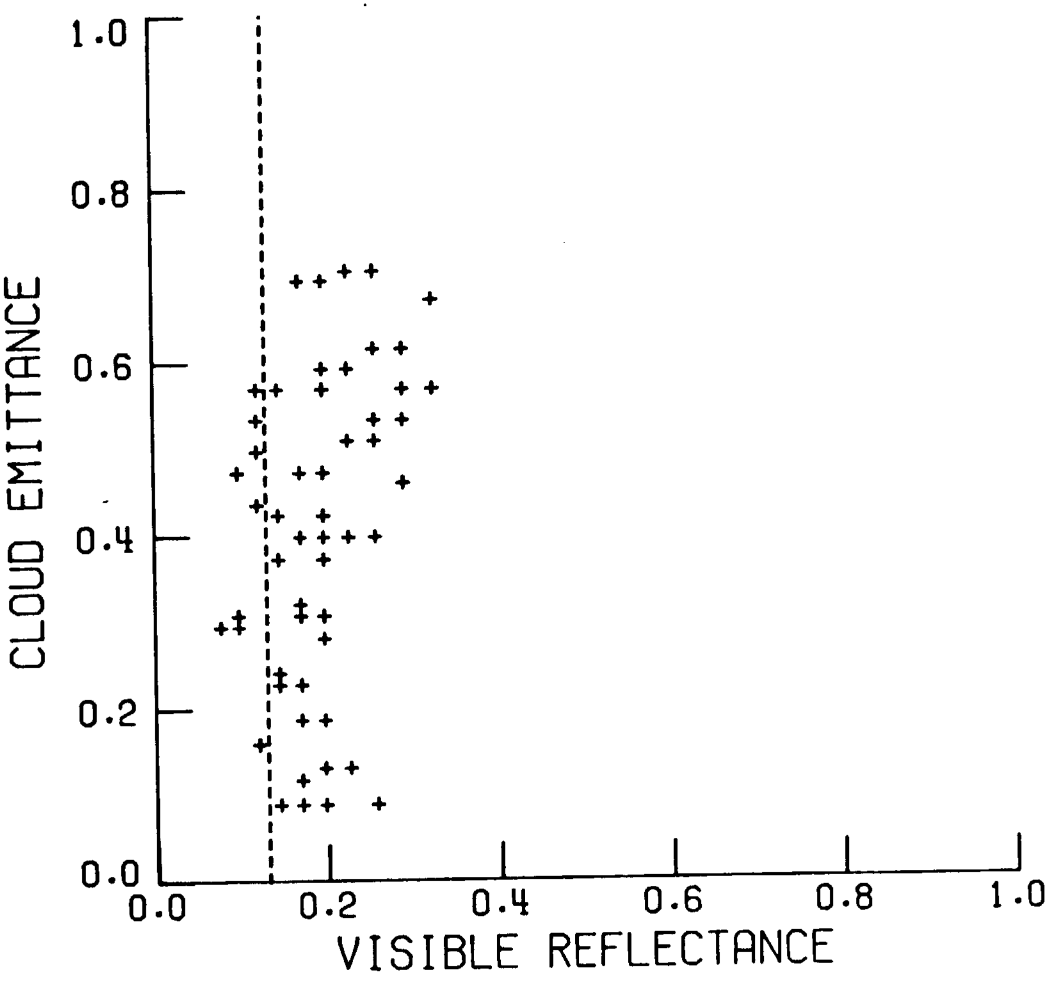
1.0
0.8
0.6
0.4
0.2
0.0
CLOUD EMITTANCE
0.0
0.2
0.4
0.6
0.8
1.0
VISIBLE REFLECTANCE

Fig. 7a

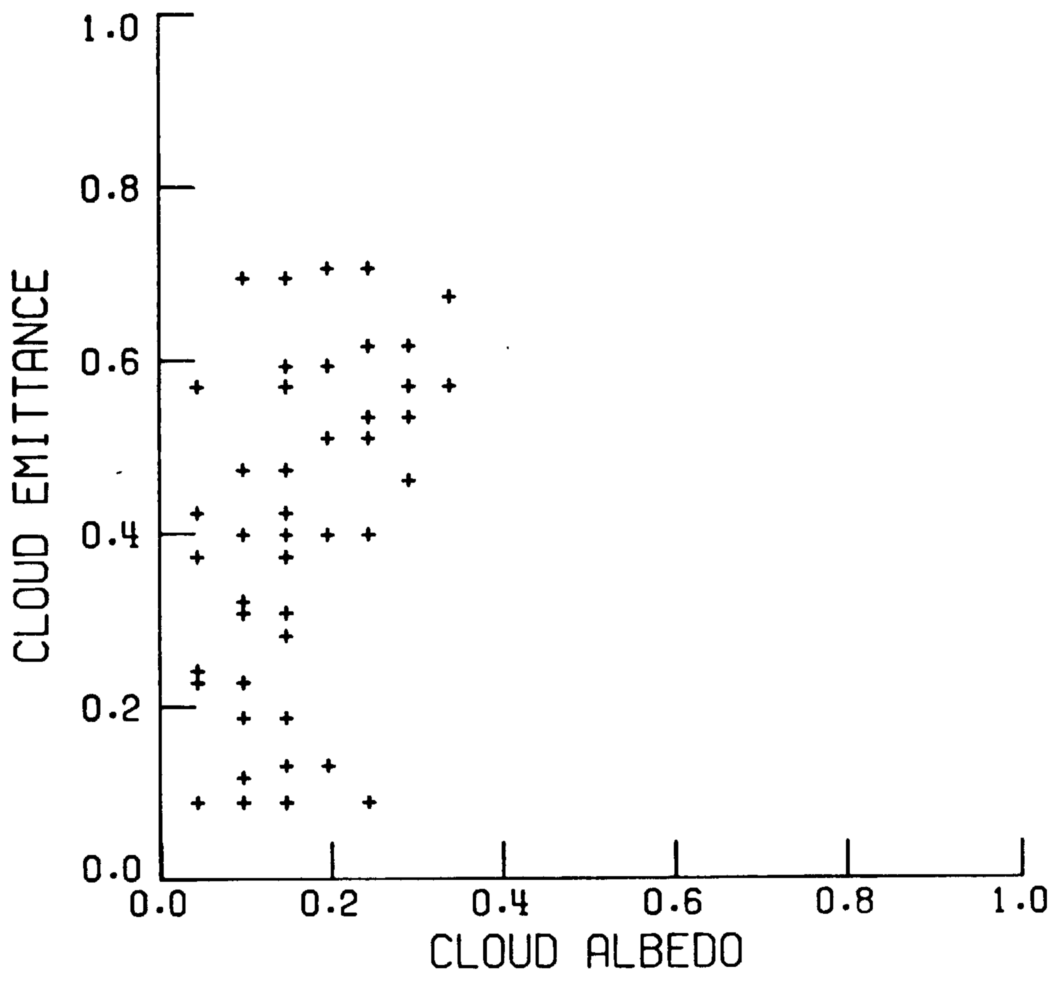

Fig 7b

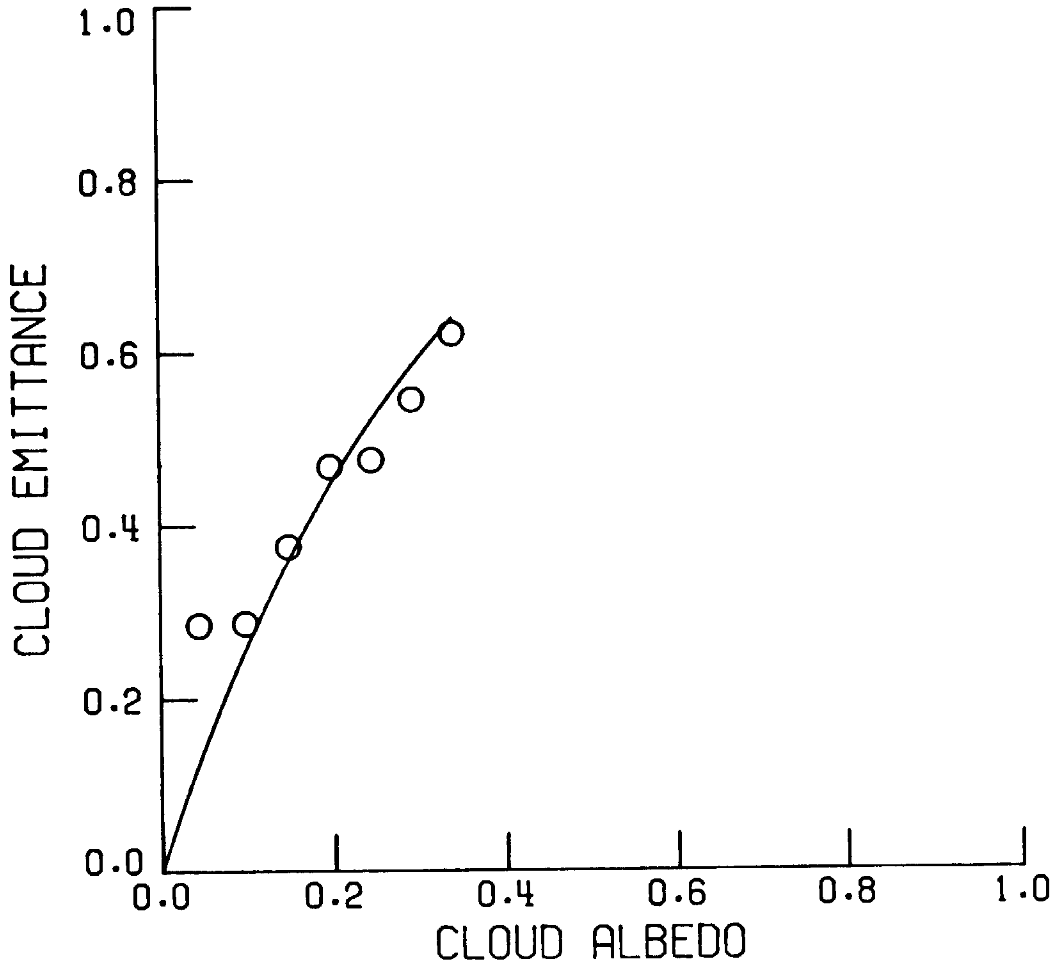

Fig. 7c

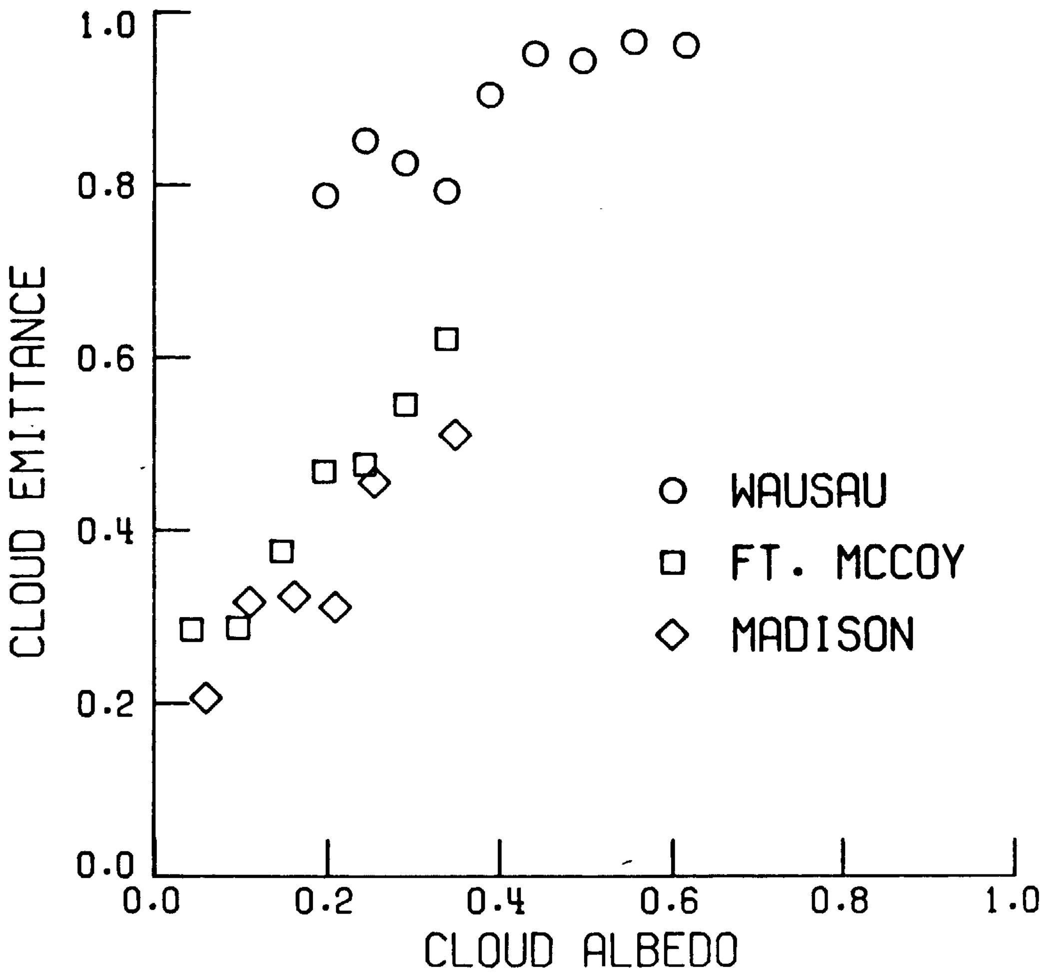
1.0
0.8
0.6
0.4
0.2
0.0
CLOUD EMITTANCE
0.0
0.2
0.4
0.6
0.8
1.0
CLOUD ALBEDO
○ WAUSAU
□ FT. MCCOY
◇ MADISON

Fig. 8

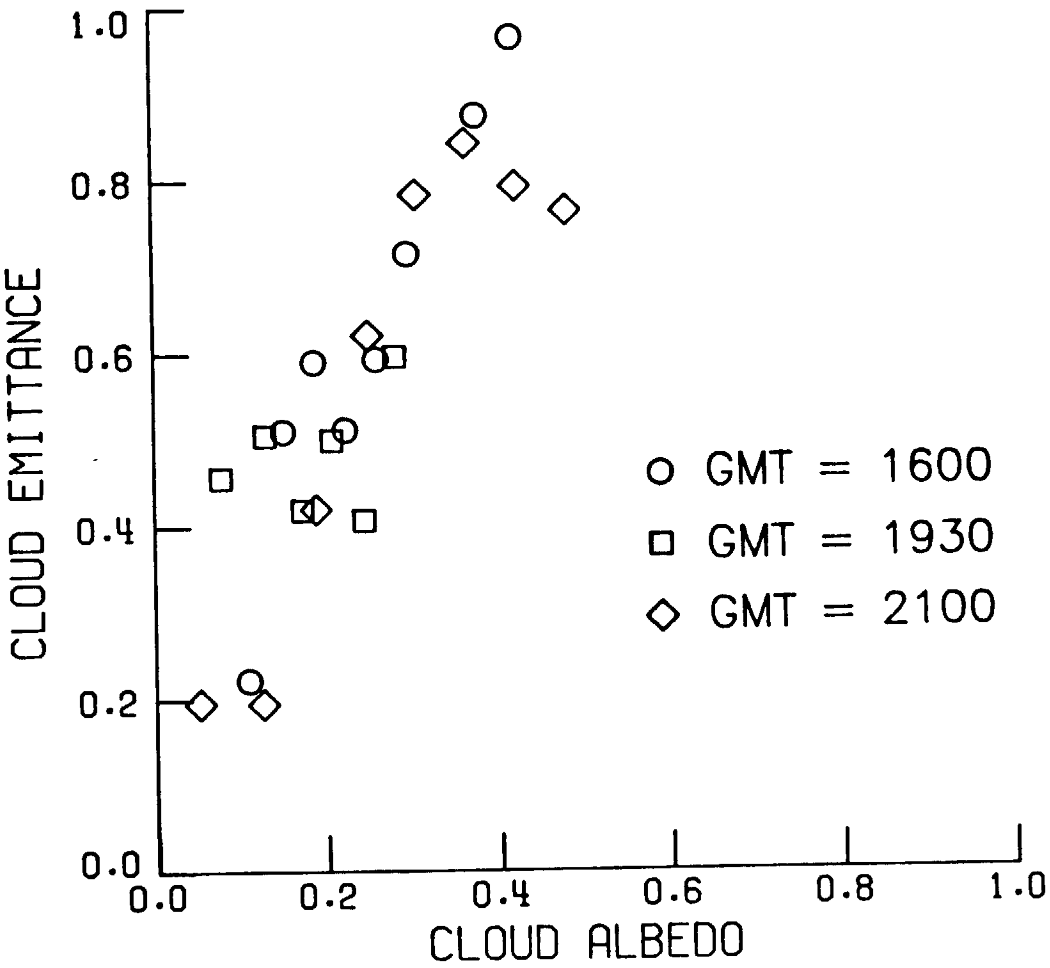
1.0
0.8
0.6
0.4
0.2
0.0
CLOUD EMITTANCE
0.0
0.2
0.4
0.6
0.8
1.0
CLOUD ALBEDO
○ GMT = 1600
□ GMT = 1930
◇ GMT = 2100

Fig. 9

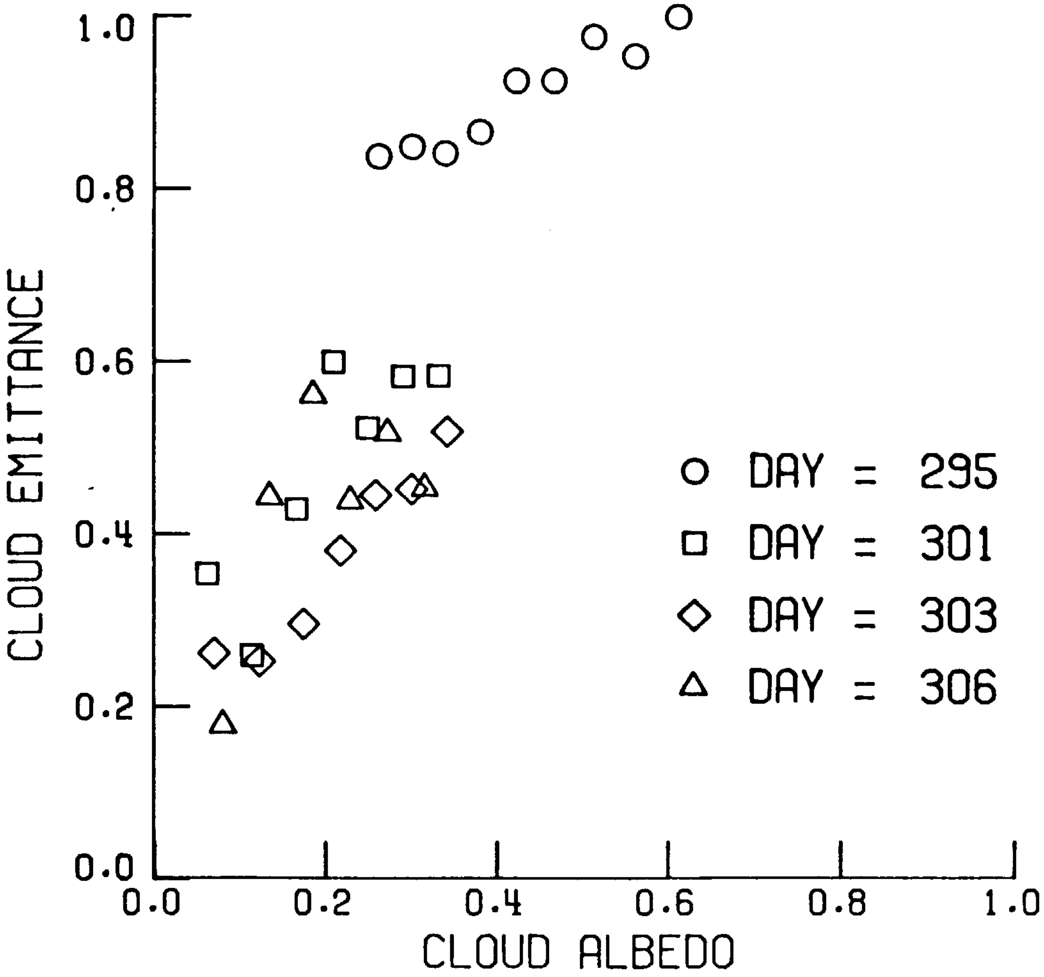
1.0
0.8
0.6
0.4
0.2
0.0
CLOUD EMITTANCE
0.0
0.2
0.4
0.6
0.8
1.0
CLOUD ALBEDO
○ DAY = 295
□ DAY = 301
◇ DAY = 303
△ DAY = 306

Fig. 10

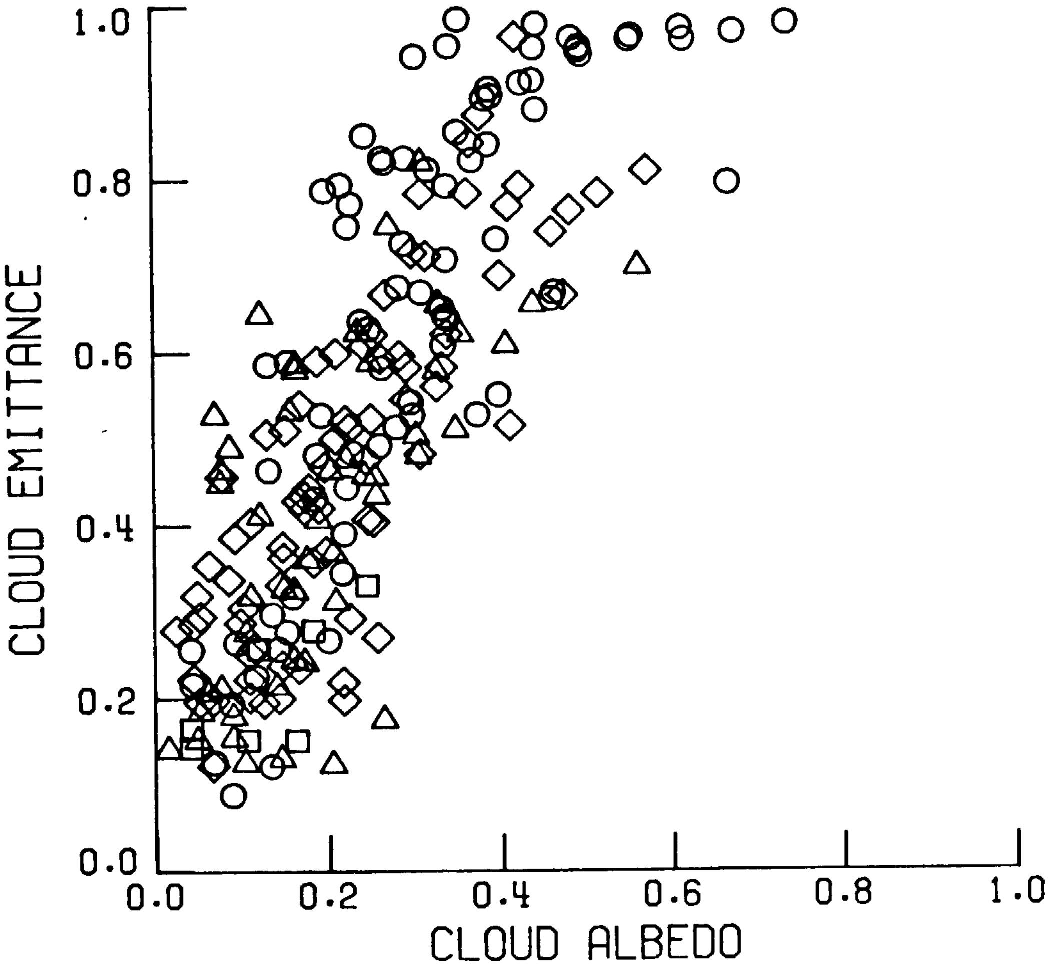

Fig. 11a

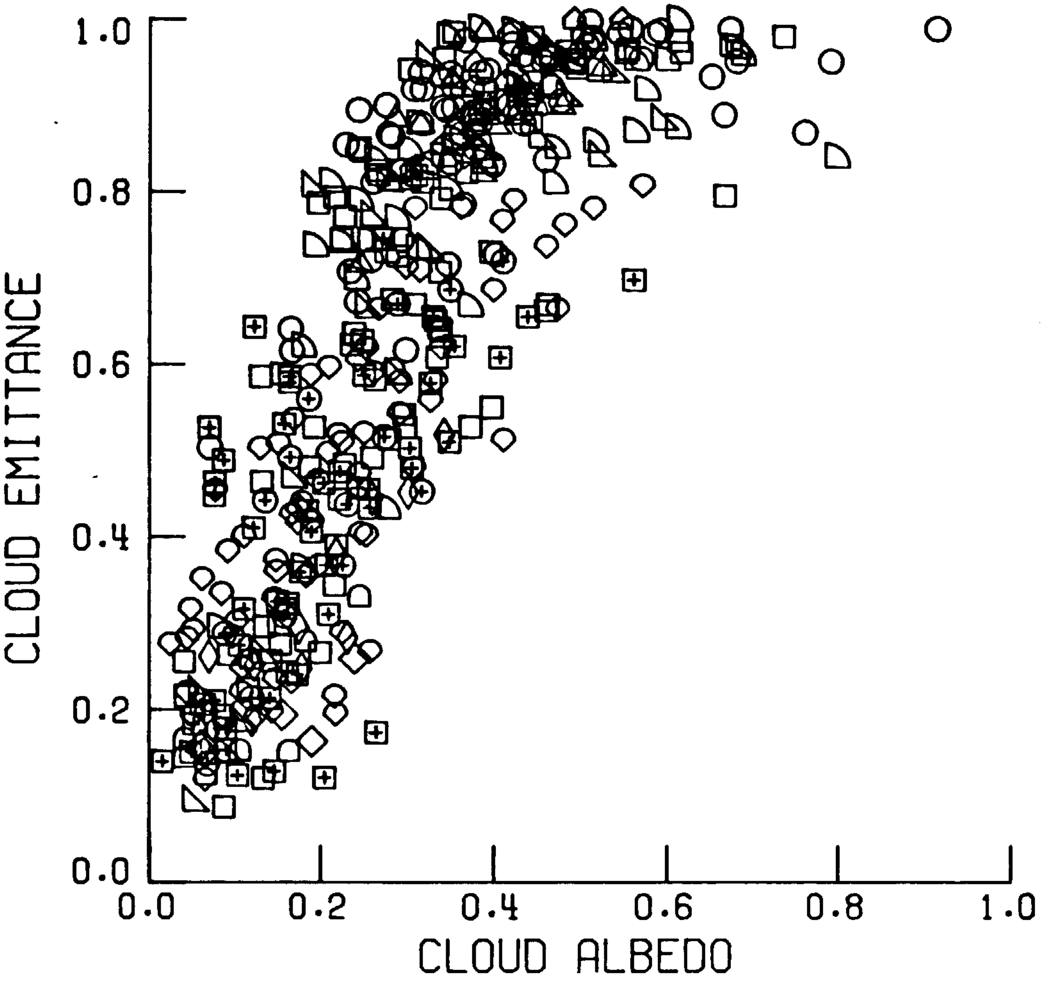

Fig. 11b

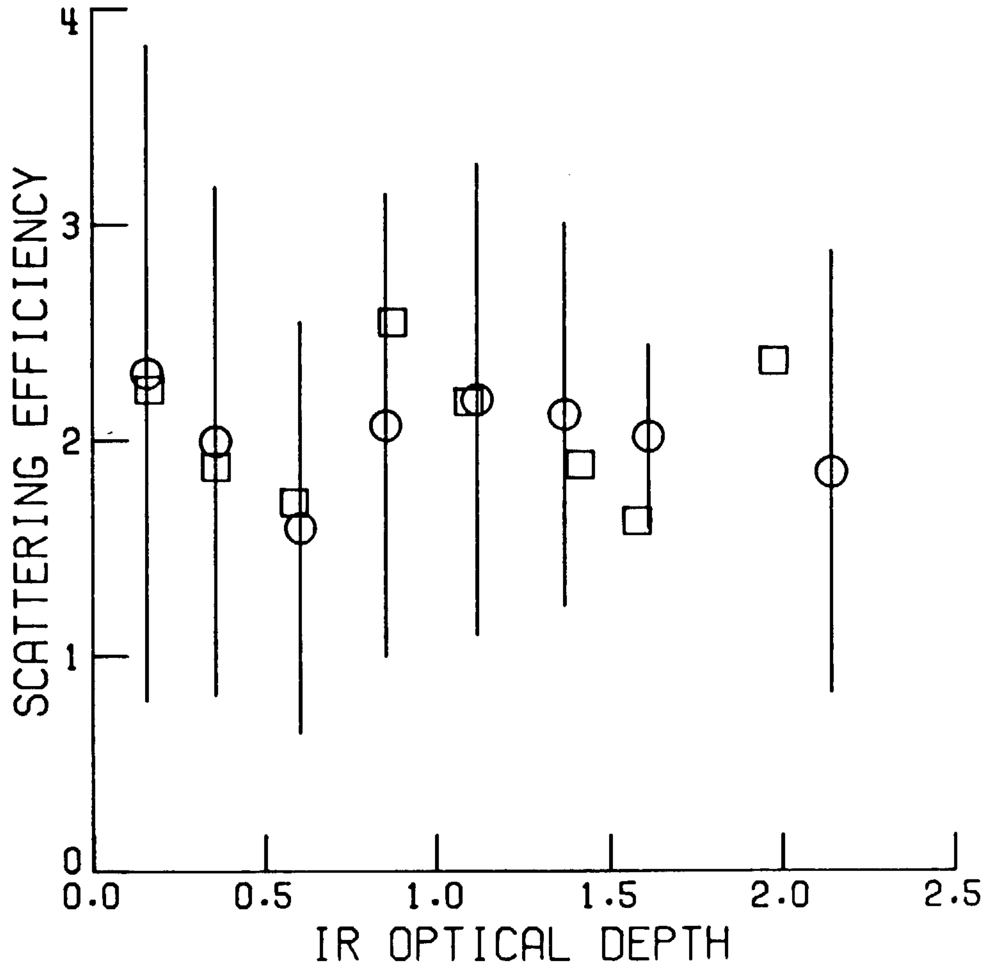
4
3
2
1
0
SCATTERING EFFICIENCY
0.0
0.5
1.0
1.5
2.0
2.5
IR OPTICAL DEPTH

Fig. 12

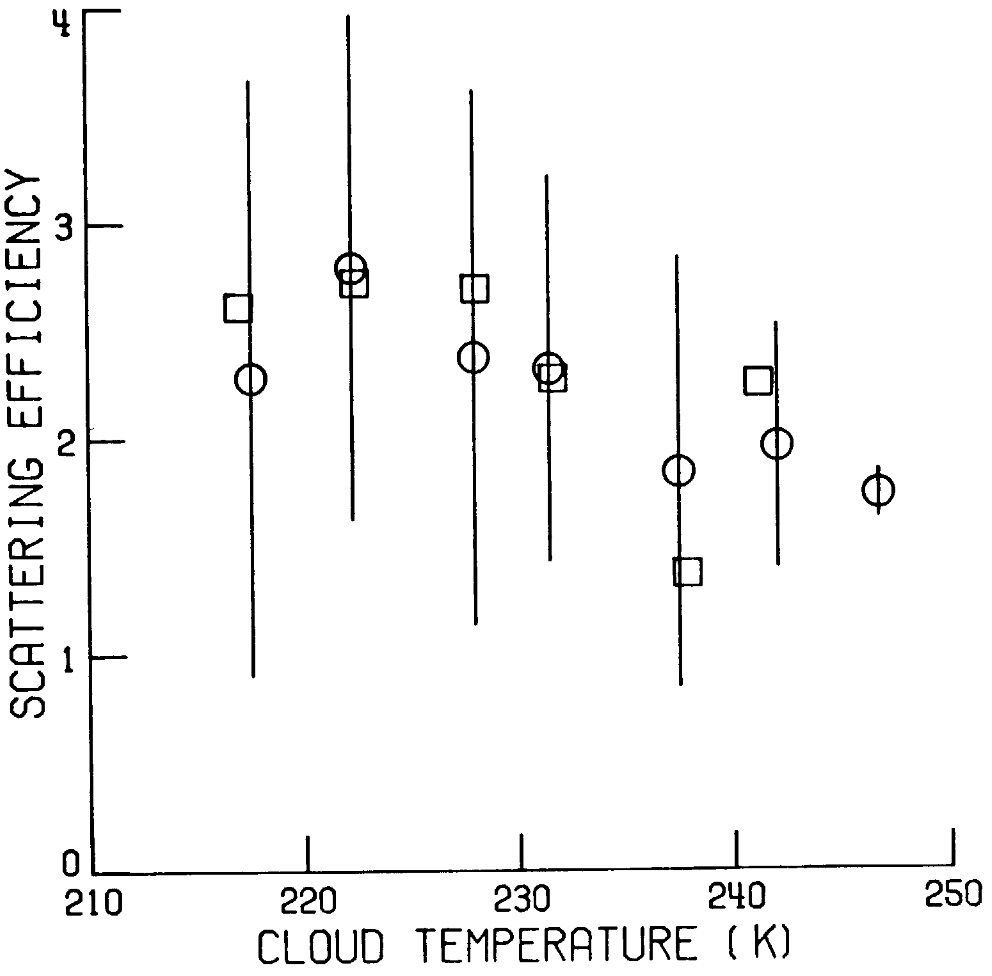
4
3
2
1
0
SCATTERING EFFICIENCY
210
220
230
240
250
CLOUD TEMPERATURE (K)

Fig. 13

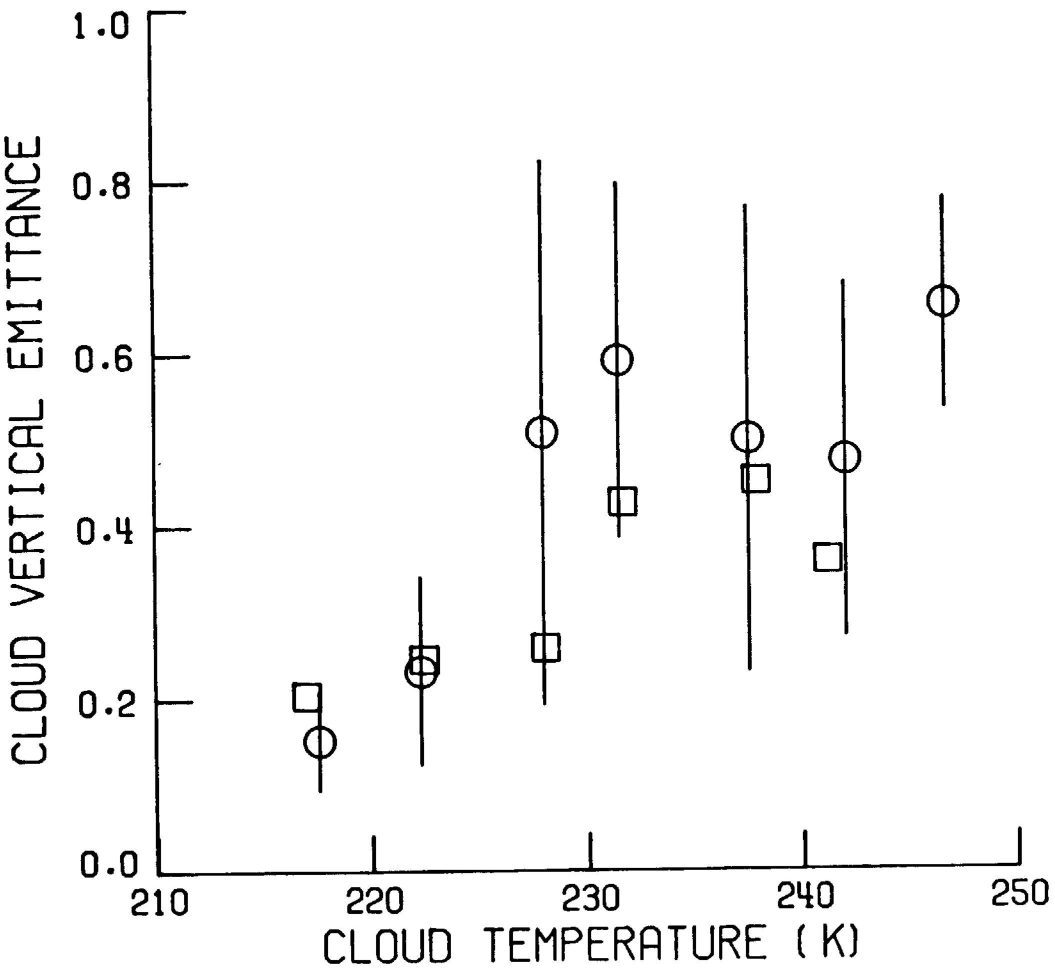
CLOUD VERTICAL EMITTANCE
1.0
0.8
0.6
0.4
0.2
0.0
210
220
230
240
250
CLOUD TEMPERATURE (K)

Fig. 14

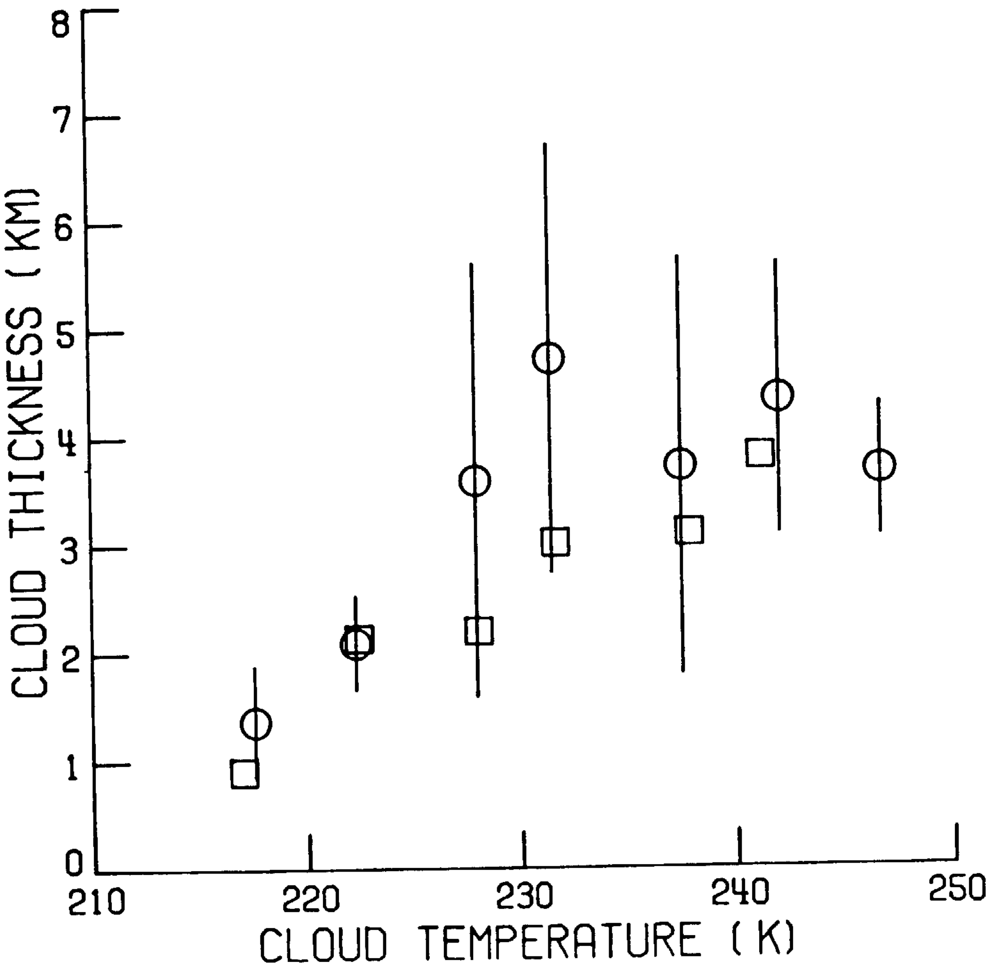
8
7
6
5
4
3
2
1
0
CLOUD THICKNESS (KM)
210
220
230
240
250
CLOUD TEMPERATURE (K)

Fig. 15

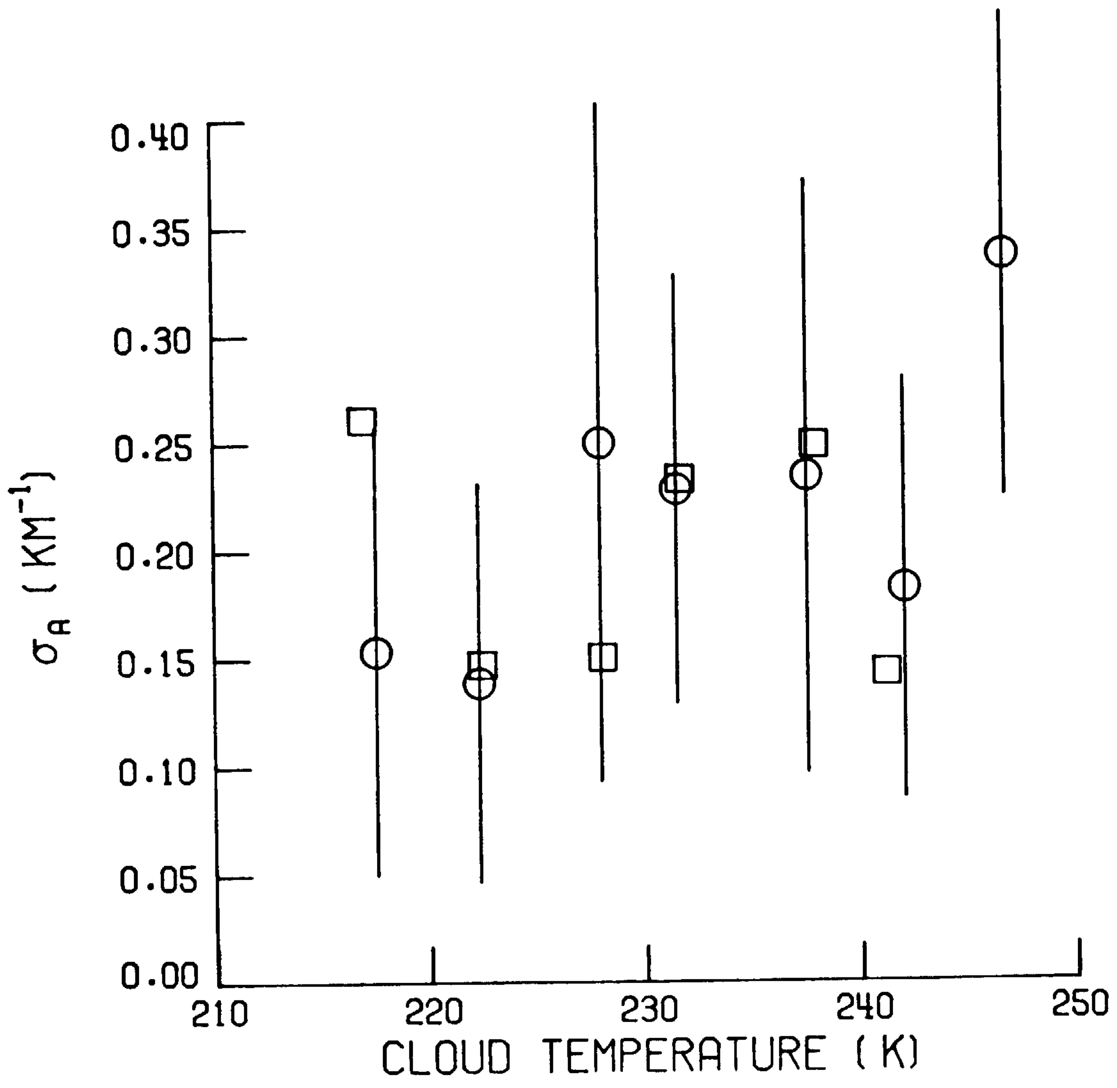
0.40
0.35
0.30
0.25
0.20
0.15
0.10
0.05
0.00
σ_a (KM^{-1})
210
220
230
240
250
CLOUD TEMPERATURE (K)

Fig. 16

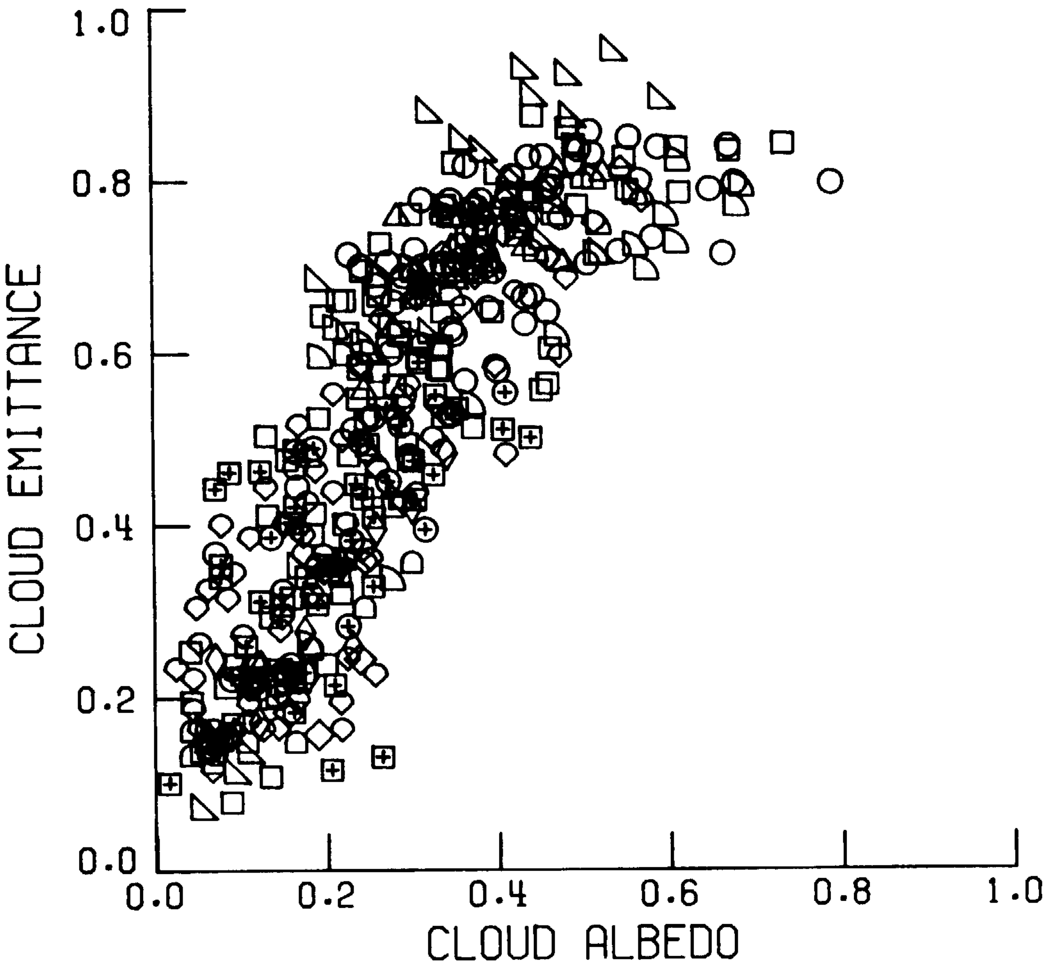

FIG, 17

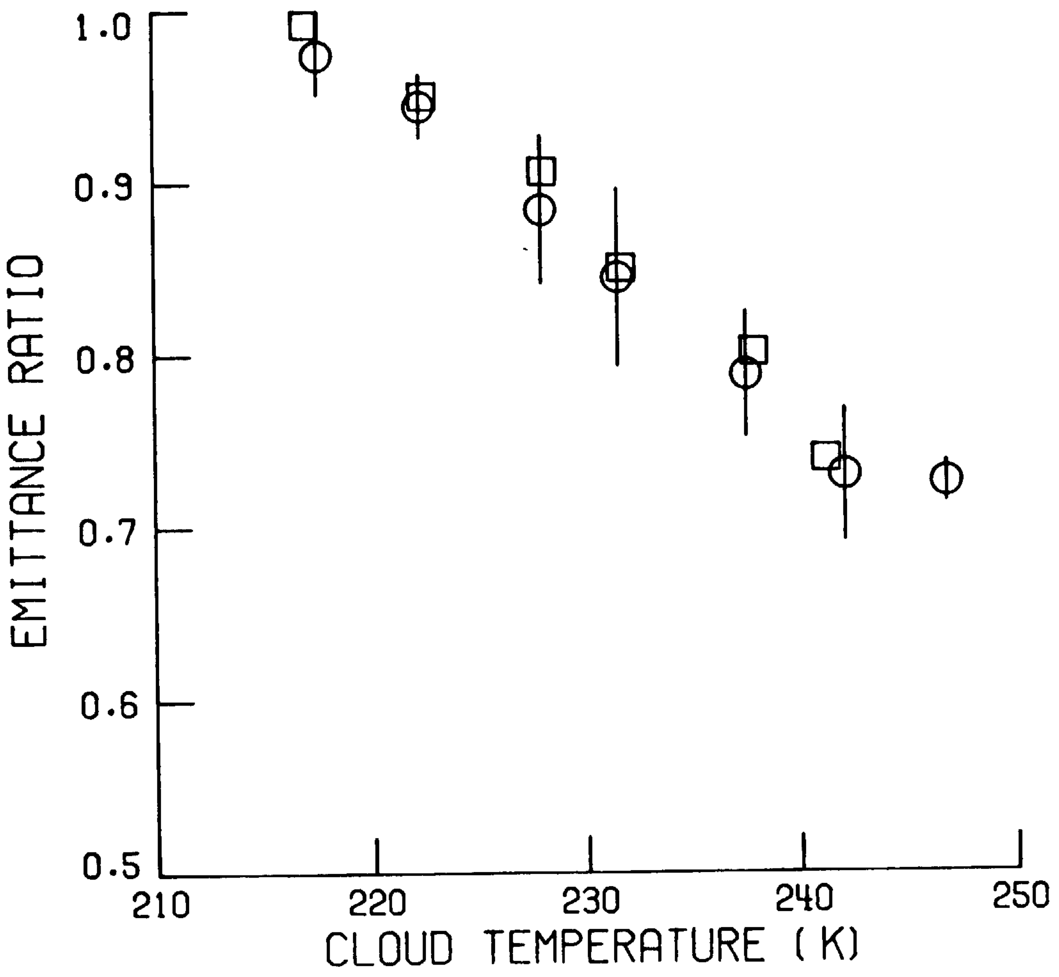
1.0
0.9
0.8
0.7
0.6
0.5
EMITTANCE RATIO
210
220
230
240
250
CLOUD TEMPERATURE (K)

Fig. 18

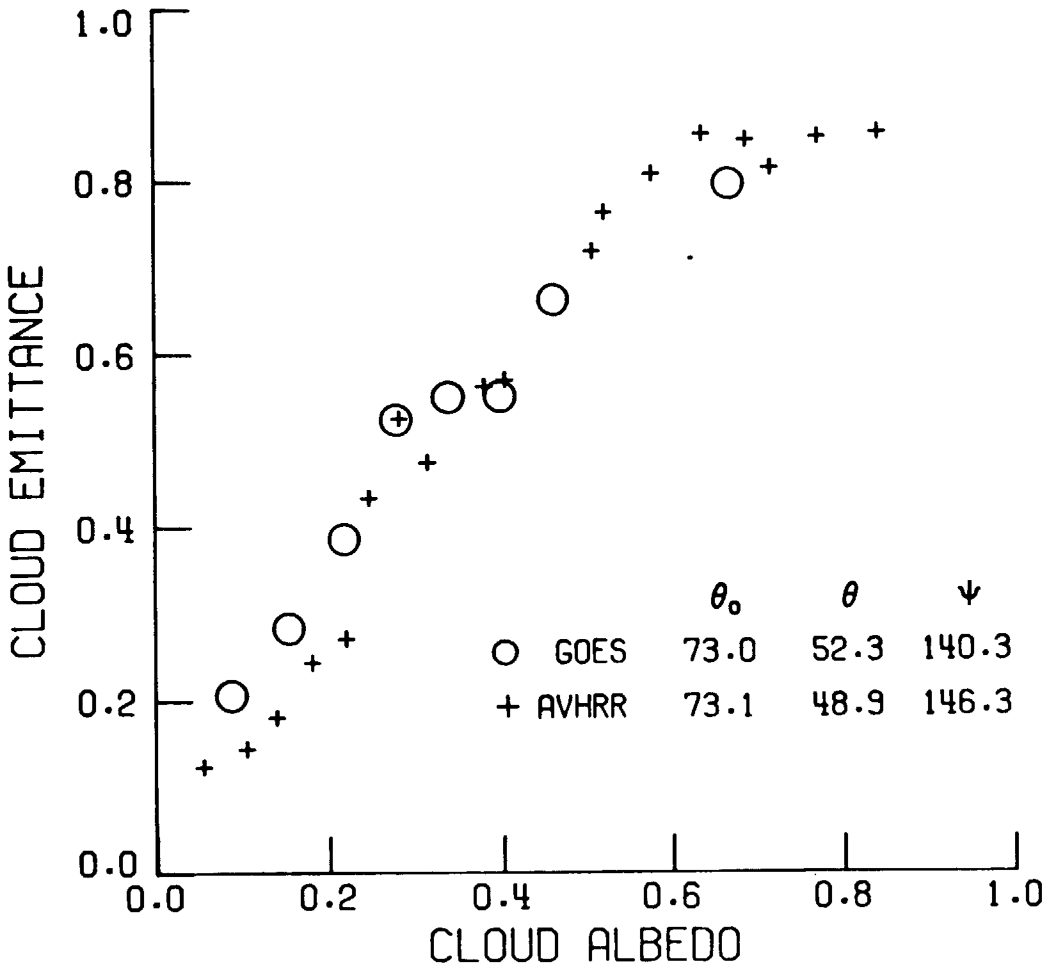
1.0
0.8
0.6
0.4
0.2
0.0
CLOUD EMITTANCE
0.0
0.2
0.4
0.6
0.8
1.0
CLOUD ALBEDO
θ₀
θ
ψ
○ GOES 73.0 52.3 140.3
+ AVHRR 73.1 48.9 146.3

Fig. 19

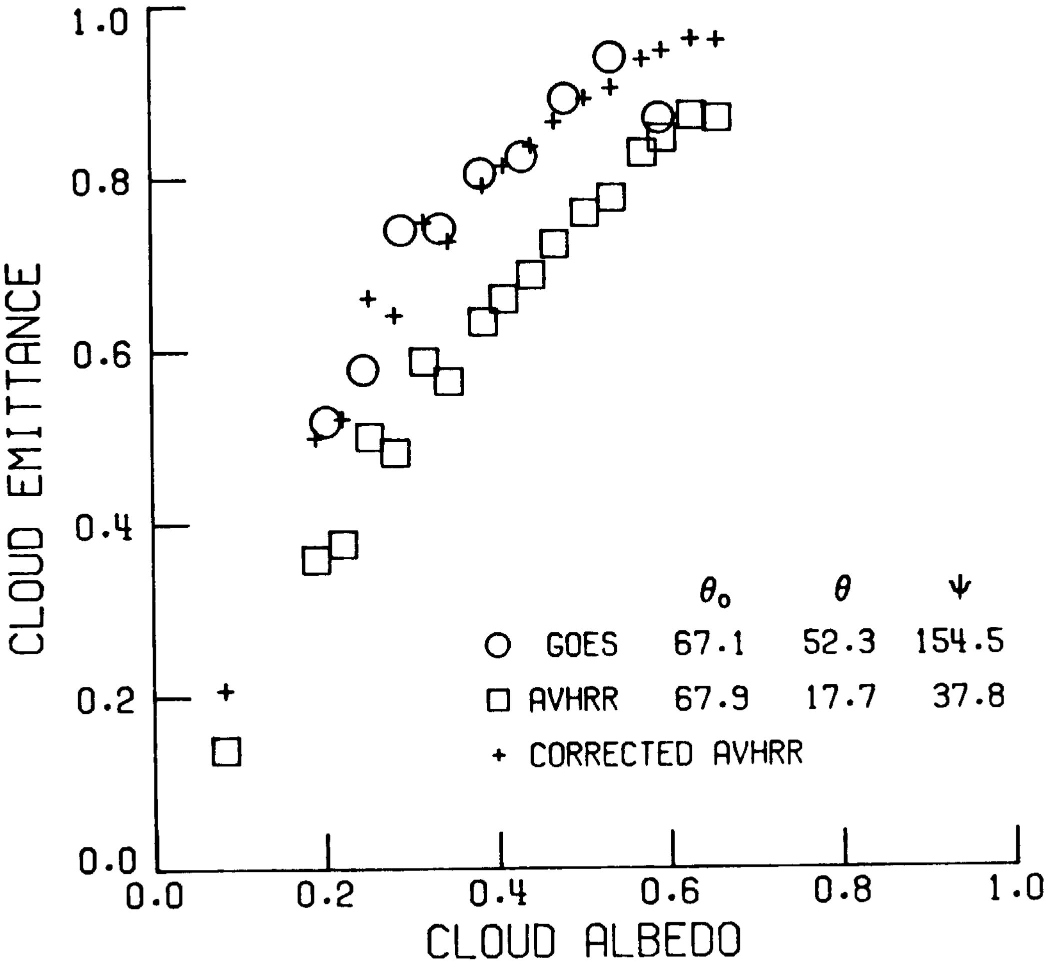

1.0
0.8
0.6
0.4
0.2
0.0
CLOUD EMITTANCE
0.0
0.2
0.4
0.6
0.8
1.0
CLOUD ALBEDO
θ_0 θ ψ
○ GOES 67.1 52.3 154.5
□ AVHRR 67.9 17.7 37.8
+ CORRECTED AVHRR

Fig. 20

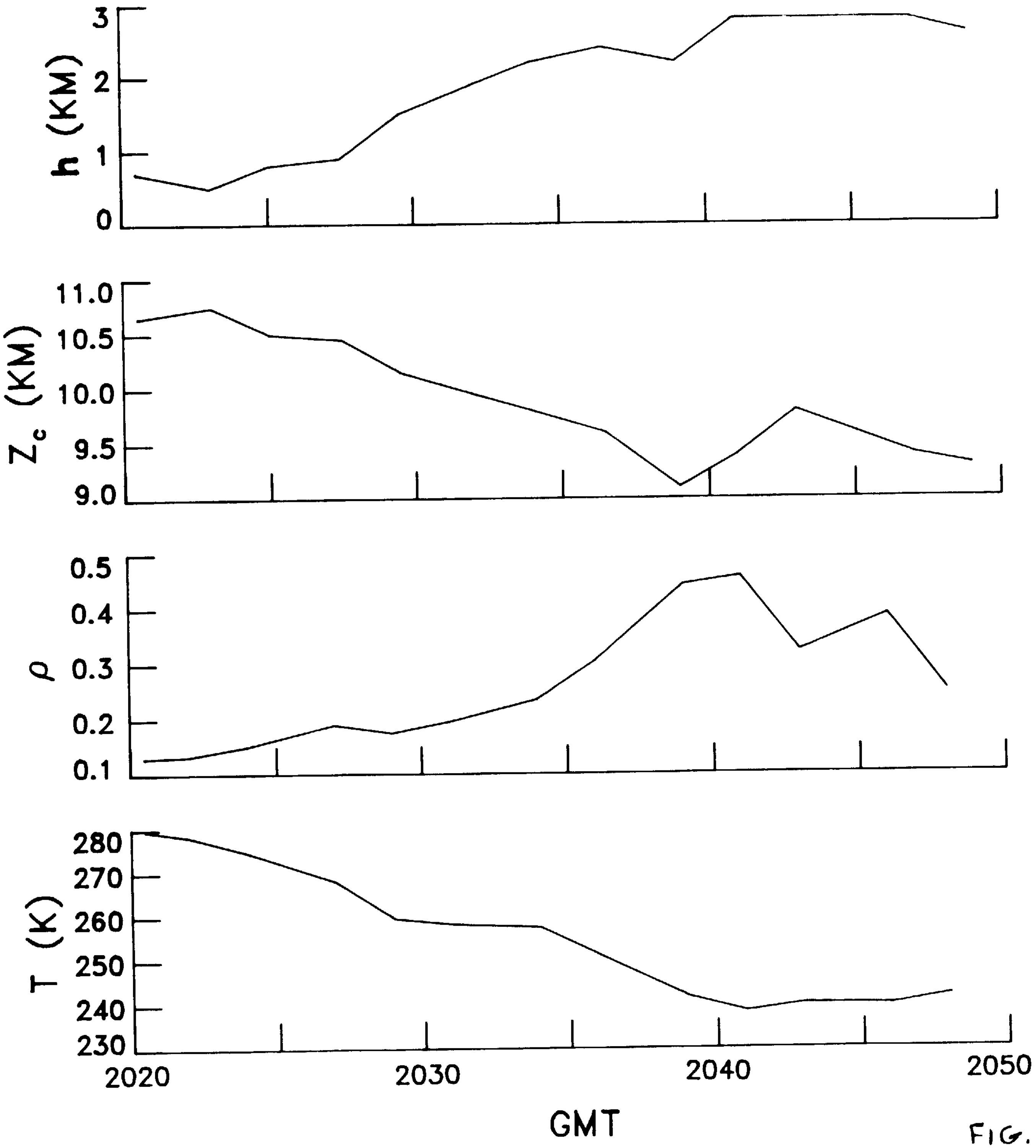

h (KM)
0
1
2
3
Z_c (KM)
9.0
9.5
10.0
10.5
11.0
ρ
0.1
0.2
0.3
0.4
0.5
T (K)
230
240
250
260
270
280
2020
2030
2040
2050
GMT

FIG. 21

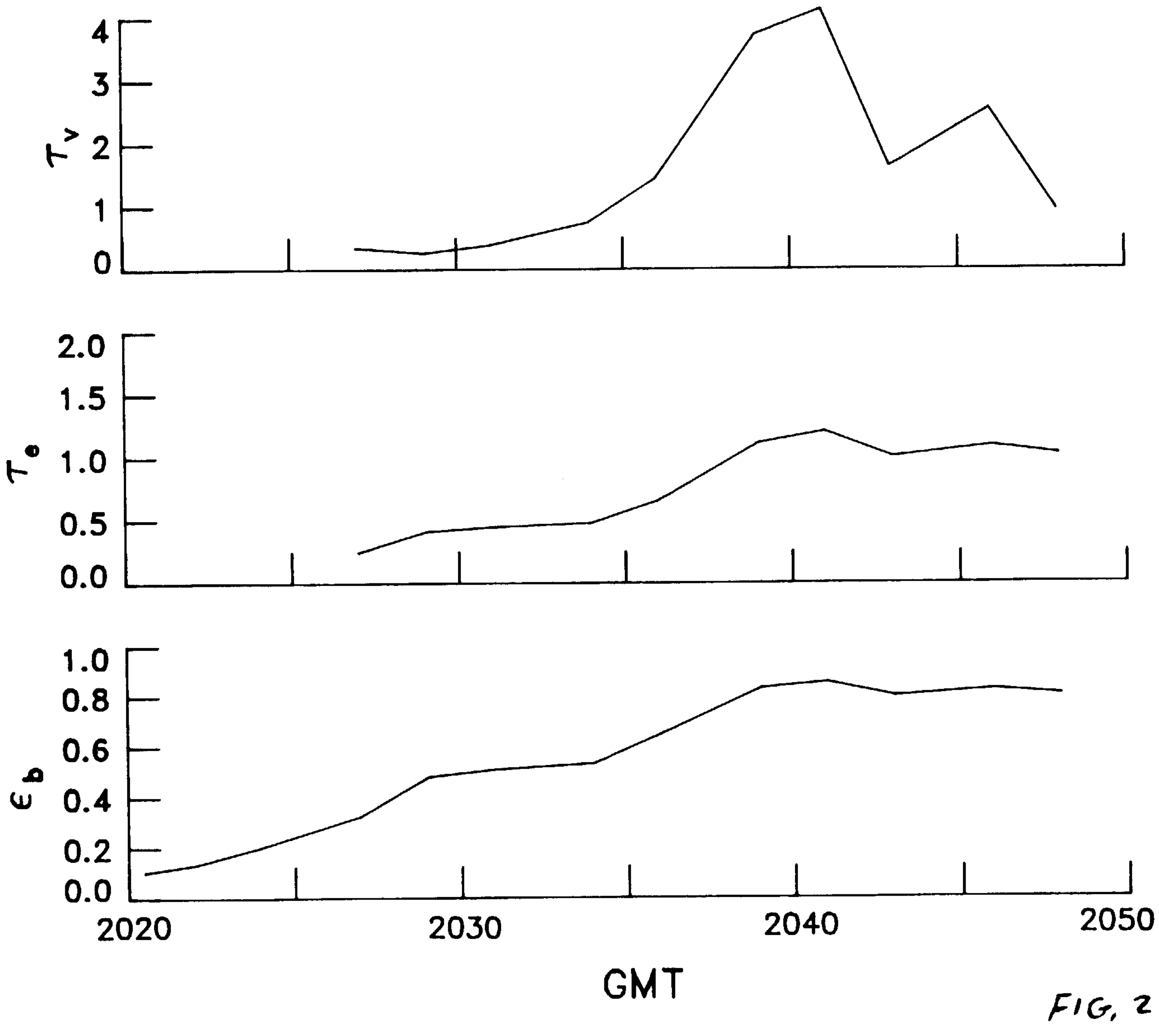
τ_v
4
3
2
1
0
τ_e
2.0
1.5
1.0
0.5
0.0
ϵ_b
1.0
0.8
0.6
0.4
0.2
0.0
2020
2030
2040
2050
GMT

FIG, 22

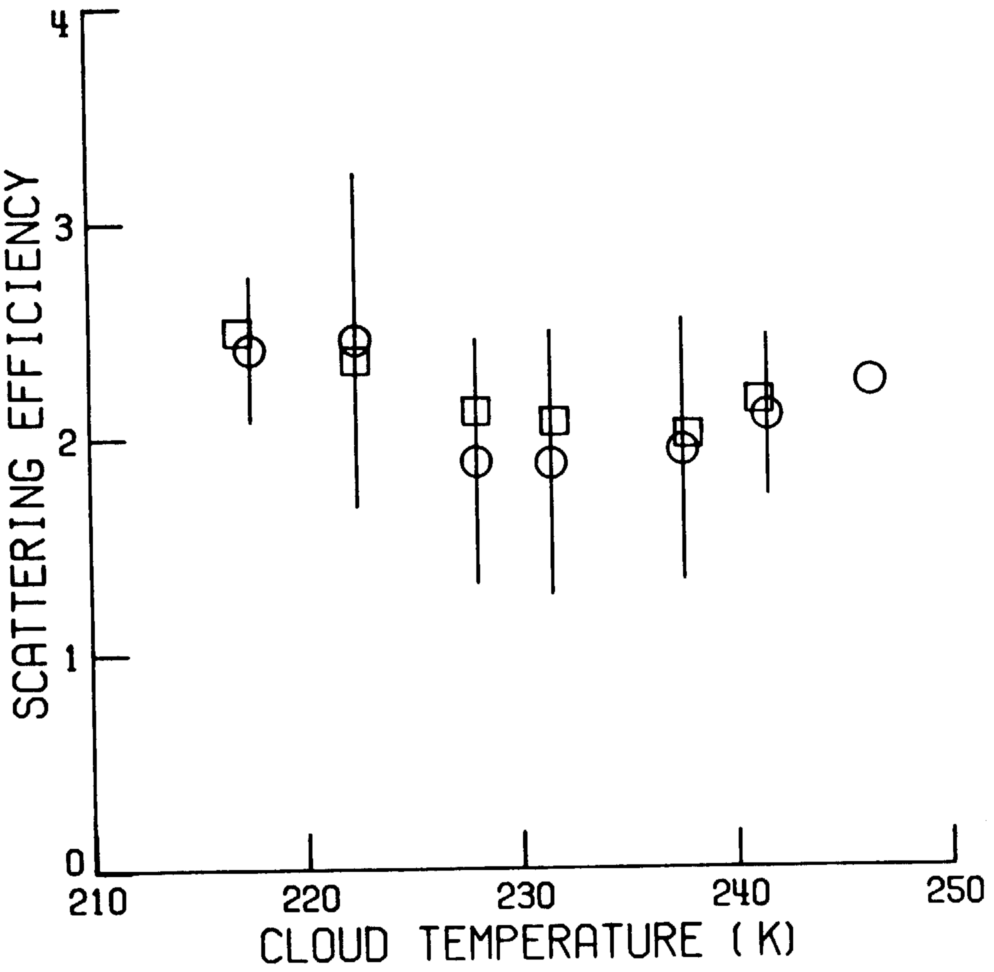
4
3
2
1
0
SCATTERING EFFICIENCY
210
220
230
240
250
CLOUD TEMPERATURE (K)

FIG. 23

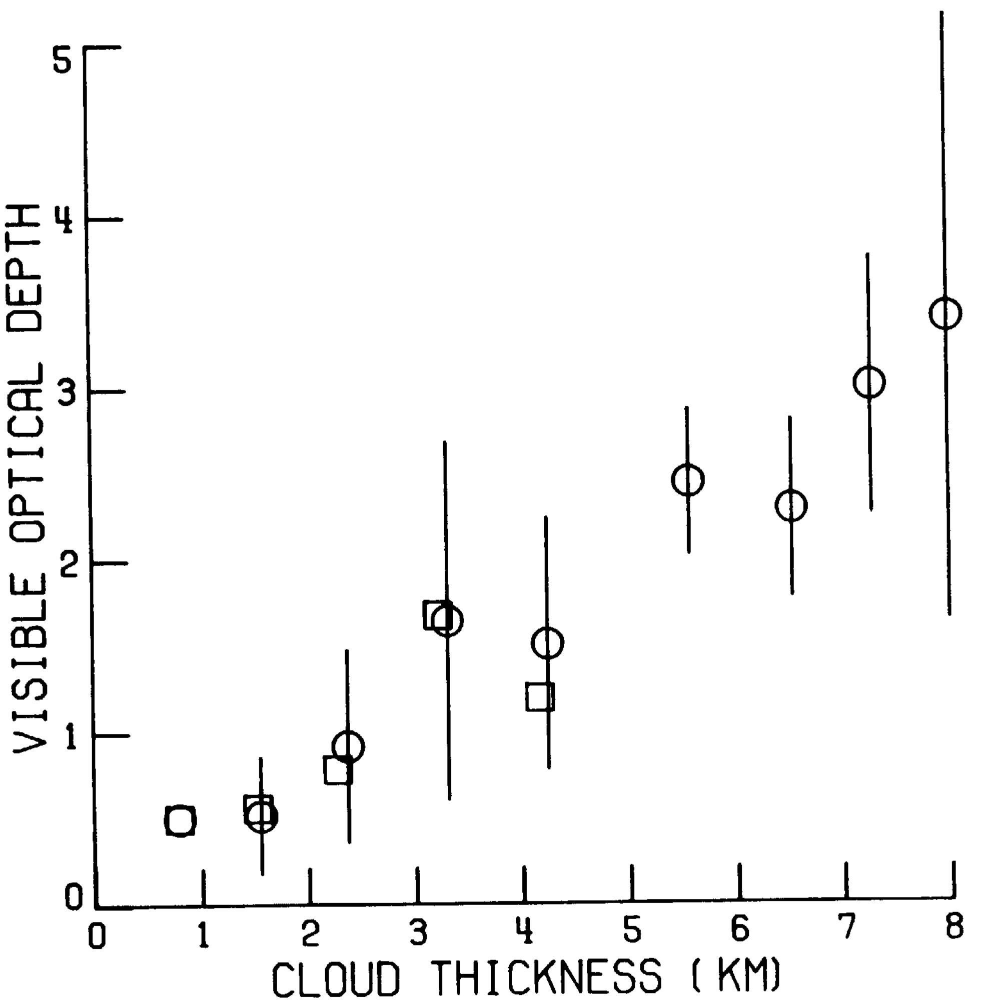
VISIBLE OPTICAL DEPTH
0
1
2
3
4
5
0
1
2
3
4
5
6
7
8
CLOUD THICKNESS (KM)

FIG. 24

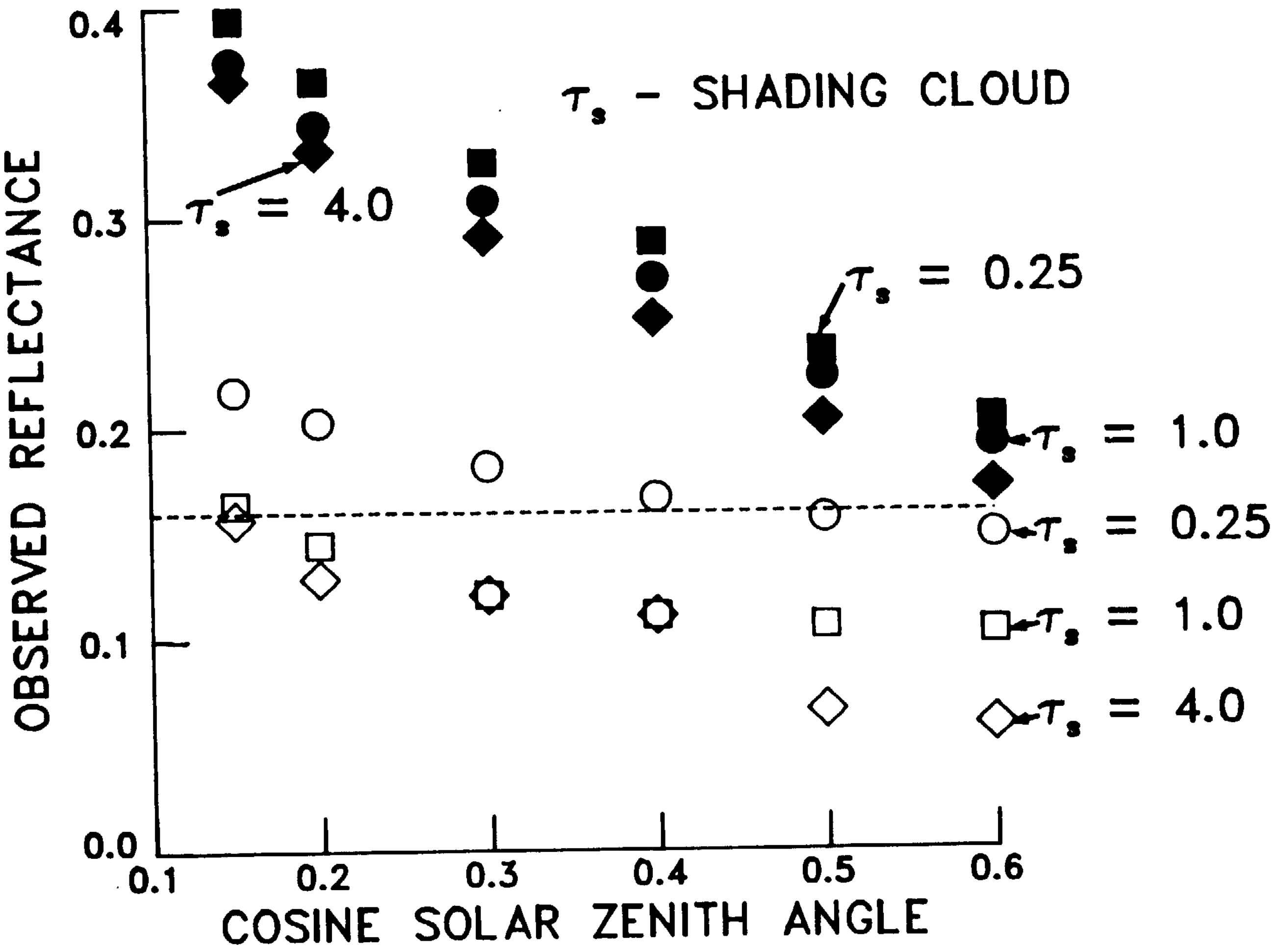

0.4
0.3
0.2
0.1
0.0
0.1
0.2
0.3
0.4
0.5
0.6
OBSERVED REFLECTANCE
COSINE SOLAR ZENITH ANGLE
τ_s - SHADING CLOUD
τ_s = 4.0
τ_s = 0.25
τ_s = 1.0
τ_s = 0.25
τ_s = 1.0
τ_s = 4.0

FiG. 25

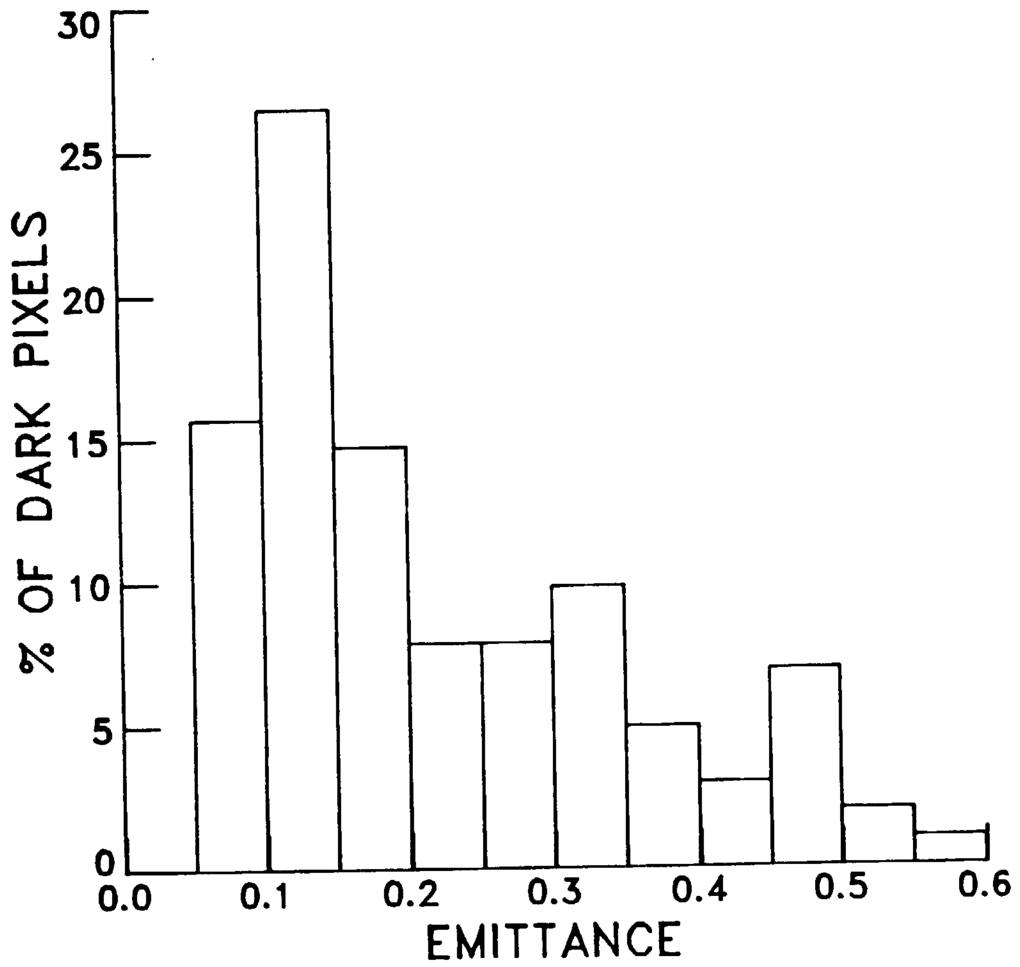

FIG. 26